Space Science Reviews (2025) 221:124
https://doi.org/10.1007/s11214-025-01253-8

Check for updates

The Radio Science Experiment on Hera, Juventas and Milani

Paolo Tortora[1,2] · **Edoardo Gramigna**[2] · **Riccardo Lasagni Manghi**[1,2] · **Marco Zannoni**[1,2] · **Ryan S. Park**[3] · **Giacomo Tommei**[4] · **Sebastien Le Maistre**[5,6] · **Ozgur Karatekin**[5] · **Giacomo Lari**[4] · **Roberto Paoli**[4] · **Maddalena Mochi**[4] · **Alfonso Caldiero**[5] · **Paolo Concari**[7] · **Daniel J. Scheeres**[8] · **Patrick Michel**[9] · **Michael Kueppers**[10]

Received: 5 November 2024 / Accepted: 25 November 2025

Abstract
Hera, the European Space Agency's first planetary defence mission, complements NASA's DART mission as part of the Asteroid Impact and Deflection Assessment collaboration. Its primary objective is to conduct a detailed post-impact analysis of the Didymos binary asteroid system, with a focus on Dimorphos, the smaller moon impacted by DART. Hera will assess the effectiveness of the kinetic impactor technique for asteroid deflection while investigating the physical and compositional properties of Dimorphos. The mission's radio science experimental setup includes an X-band radio link enabling two-way range and range-rate measurements as well as Delta-DOR observations, complemented by additional data from inter-satellite ranging with the Juventas and Milani CubeSats, optical navigation imaging, and altimetry. These measurements will enhance the accuracy of the post-impact data analysis. This paper summarizes the existing literature, outlines the experimental configuration and mission operations during the cruise phase and at the Didymos system, and discusses the expected scientific outcomes of Hera's radio science experiment.

1 Introduction

A specific category of Near Earth Asteroids (NEAs) celestial bodies, known as Potentially Hazardous Asteroids (PHAs), presents a potential threat to Earth due to the risk of significant damage upon impact. PHAs are characterized by a mean diameter exceeding 140 meters and a minimum orbit intersection distance to Earth less than 0.05 Astronomical Unit (AU) (Perna et al. 2013). With the continuous expansion of our knowledge about Near-Earth Objects (NEOs) over the past decades, our understanding of the true statistical probability of a potentially catastrophic event has also increased, albeit remaining at a very low likelihood. Nevertheless, being prepared for such events is crucial, as it may be the only means to ensure the survival of humankind.

In the context of planetary defence missions, the objective is to prevent the impact of PHAs, employing various techniques. For asteroids of sizes of a few hundreds meters at most, where the likelihood of Earth impact is deemed higher (Ivanov and Hartmann 2007), the most efficient deflection technique involves the impact of a rocket-launched spacecraft, the so-called kinetic impactor technique. In this context, the first two humankind planetary

Extended author information available on the last page of the article

Published online: 03 December 2025

Fig. 1 Didymos binary asteroid system, showing the central body Didymos on the right (∼780 m diameter), and the secondary body Dimorphos on the left (∼151 m diameter). This is a real image of the Didymos system taken by DART DRACO camera mosaics. Image credit: NASA/Johns Hopkins APL, https://dart.jhuapl.edu/Gallery/

Table 1 Didymos system and Dimorphos orbital parameters. The base reference frame is the Earth Mean Orbit at J2000 (EMO2000)

Didymos system	
GM system	4.0417×10^{-8} km^3/s^2
GM Didymos	4.0071×10^{-8} km^3/s^2
GM Dimorphos	3.4522×10^{-10} km^3/s^2
Semimajor axis	1.643 AU
Orbital period	2.109 years
Eccentricity	0.384
Inclination (EMO2000)	3.414 deg
Dimorphos	
Semimajor axis	1.2 km
Orbital period	11.9215 h (pre-impact); 11.3685 h (post-impact)
Eccentricity	$<$ 0.03 (post-impact)
Inclination (EMO2000)	169.3 deg

defence space missions are the DART (NASA) (Cheng et al. 2018) and Hera (ESA) missions (Michel et al. 2022, 2025). Together, they constitute the Asteroid Impact and Deflection Assessment (AIDA) international collaboration (Cheng et al. 2015). The objective of this cooperation is to evaluate the feasibility and effectiveness of the kinetic impactor technique for asteroid deflection.

The target of this collaboration is the Didymos binary asteroid system (see Table 1), which includes a central body called Didymos, with a diameter of ∼780 m, and a secondary body called Dimorphos, a ∼151 m diameter asteroid orbiting Didymos, see Fig. 1. The distance between the two asteroids is roughly 1.21 km (Michel et al. 2025).

The distinctive spinning-top shape and rapid rotation of Didymos (∼2.26 h (Pravec et al. 2006; Richardson et al. 2024)) hint at a rubble-pile structure, suggesting possible formation scenarios like spin-up-driven mass loss followed by the gravitational accumulation of the secondary (Agrusa et al. 2024; Wimarsson et al. 2024), or gravitational reaccumulation after a catastrophic disruption, as described in Richardson and Walsh (2006). Hence, if Dimorphos and Didymos share a common origin, it implies that Dimorphos is also likely a rubble-pile (Agrusa et al. 2021). The highly dissipative nature of rubble-pile asteroids suggests that the system has undergone sufficient time for Dimorphos to become tidally locked

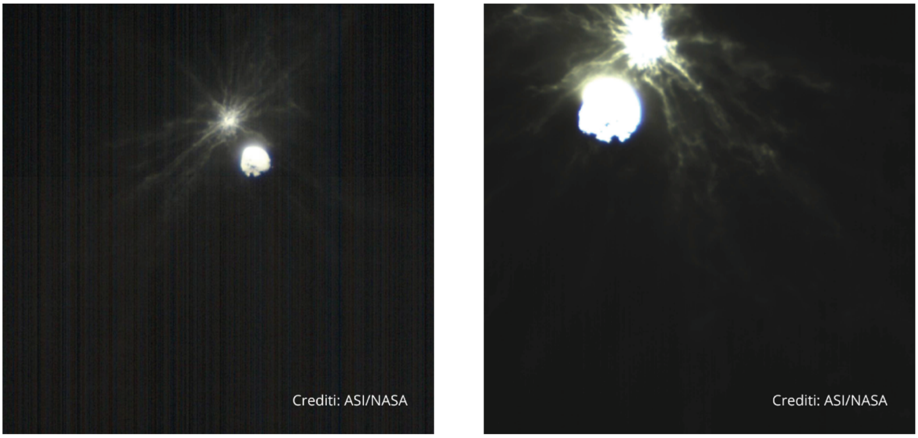

Fig. 2 LICIACube LUKE Camera image. LICIA-Dimorphos distance = 105 km (left) - 54 km (right). Image credit: ASI/NASA

and enter a dynamically relaxed state before the DART impact, in accordance with the theories proposed by Goldreich (2009) and Jacobson and Scheeres (2011).

It is important to note that the Didymos binary poses no threat to our planet Earth, and the DART mission served as a feasibility study. Therefore, the primary objective of DART was not to modify the heliocentric trajectory of the asteroid. Instead, the mission aimed to impact the secondary, causing an observable change in its orbital period around the primary. To maximize observability while minimizing propellant usage, the mission planned a retrograde impact on Dimorphos.

A few weeks after the impact, which occurred on September 26th, 2022, the DART investigation team confirmed that the spacecraft collision with its target asteroid successfully altered the orbit of Dimorphos, decreasing its orbital period by ∼33 minutes (Thomas et al. 2023; Cheng et al. 2023).

Furthermore, the Light Italian CubeSat for Imaging of Asteroids (LICIACube) (Dotto et al. 2021) deployed 15 days prior to the DART impact on Dimorphos, was able to document and witness the collision by taking images of the event and the minutes that followed (Dotto and Zinzi 2023). LICIACube captured images of the DART impact and the resulting ejecta cloud offering essential complementary insights into the impact, and playing a crucial role in characterizing the ejecta plume, see Fig. 2.

However, the combination of DART, LICIACube data, and telescope observations (Hubble Space Telescope, James Webb Telescope etc) is insufficient for a complete and accurate characterization of the final outcome. Therefore, dedicated in-situ observations, to be carried out during the Hera mission, become necessary for a comprehensive and more detailed understanding of the effect of the kinetic impact on the binary asteroid system.

Hera was successfully launched October 7th, 2024 on board a SpaceX Falcon 9 rocket. Currently on its way to the Didymos system, the spacecraft is scheduled to arrive there in October 2026 (Michel et al. 2022, 2025). Hera also carries two CubeSats, Juventas and Milani, which will be released in the proximity of the Didymos system (Goldberg et al. 2019; Karatekin et al. 2021; Ferrari et al. 2021a,b) to complement the observations of the mother spacecraft. The main objectives of Hera relate to planetary defense and deflection demonstration (Michel et al. 2022, 2025) while also contributing to asteroid science.

The Hera Radio Science Experiment (RSE) is crucial to fulfilling the core mission requirements for planetary defence, as well as being extremely relevant for asteroid science. The goal is to make a major step forward in the knowledge of the kinetic impactor technique at small bodies, in order to scale it to potentially hazardous asteroids in the future. This requires a substantial increase in the accuracy of the results obtained by DART and LICIACube. Hera's experimental setup exploits dedicated onboard and ground hardware to provide precise measurements of the spacecraft range, range-rate, and angular position (Delta-DOR), as well as additional data coming from the optical images, altimeter, and CubeSats range. We are aware that the relative precision of the gravitational parameters depends on the size of the target, and for this reason we carried out a detailed error budget (see Sect. 5) and a covariance analysis to ensure that the Hera concept of operations (CONOPS) is consistent with the objectives. The physical parameters of interest will be derived from a suitable joint analysis of the above-mentioned observable quantities.

The paper is organised as follows. Section 2 presents the Hera RSE science goals, objectives and requirements, focusing on the momentum transfer and geophysical parameters. In Sect. 3 we describe the adopted measurements for the Hera RSE investigation. Section 4 shows the architecture of the onboard and ground radio systems. Section 5 provides the error budget for all observable quantities. Section 6 describes the Hera operations during cruise and asteroid phase. Section 7 outlines the orbit determination methods employed in this investigation, as well as the numerical procedures developed for the orbit determination setup and estimation of the scientific parameters of interest (i.e., asteroids' orbits, rotational state, mass, extended gravity field, and moments of inertia). In particular, Sect. 7.1.2 describes the full two-body problem, a higher accuracy dynamical model which accounts for the full coupling between the asteroids' translational and rotational motion, and developed for the Hera RSE. Furthermore, Sect. 7.1.3 provides an overview of the main expected non-gravitational accelerations and relative models. Finally, Sect. 8 presents the expected accuracies for geodesy and geophysics of Didymos and Dimorphos, relevant to characterize the kinetic impactor technique, while Sect. 9 describes the Hera data archiving and distribution plan.

2 Hera RSE Science Goals

The main RSE objectives and requirements are:

1. Determine accurate reconstructed trajectory for Hera, Juventas, and Milani.
2. Estimate the mass and extended gravity fields of Didymos and Dimorphos, to constrain their interior structures and global properties (e.g., size, shape, volume, density, porosity). Dimorphos' mass shall be estimated with a relative error of at most 10%, with a goal of 1%, which will allow the momentum enhancement factor estimation (Meyer et al. 2023; Feldhacker et al. 2017).
3. Characterize the post-impact mutual orbits, rotational states, and dynamics of the binary system. Specific requirements include an absolute accuracy of 5 m in the semi-major axis (with a goal of 1 m), eccentricity accuracy of better than 0.001, spin rate accuracy of Dimorphos with accuracy better than 0.1%, and spin pole of Didymos and Dimorphos with accuracy better than 1 degree (with a goal of 0.1 degrees).
4. Estimate the rotational state, including librations, of Dimorphos, which is crucial for determining the energy dissipation of the system, post-impact dynamics, and further constraining its interior structure. The orbital parameters of Dimorphos and its librations are directly related to the energy dissipation of the system (Meyer et al. 2023). The phase of

the libration can also be helpful to constrain the dissipation, since the tidal quality factor Q is a function of the phase lag, $\Delta\phi$ (i.e., $Q^{-1} = \sin(\Delta\phi)$), which represents a constant misalignment of the tidal bulge (e.g. Le Maistre et al. 2013).

Using Hera data, the mass of Didymos and Dimorphos can be estimated with high accuracy. Combined with their shape models, the bulk density of the two bodies (and thus their density difference) can be computed, which provides constraints on their interior structure. Moreover, as a byproduct of an accurate reconstruction of the trajectory of Hera during selected close encounters with the Didymos-Dimorphos system, the asteroids' gravity field could be obtained with a resolution and accuracy that would allow us to constrain their large-scale internal mass distribution. For that, the role of the two CubeSats will be essential as shown by Gramigna et al. (2024b).

Juventas and Milani CubeSats will be tracked by Hera via an Inter-Satellite Link (ISL) system, the first miniaturized satellite-to-satellite transceiver ever flown in deep space. This represents a crucial addition to the gravity investigation, as the relative motion between Hera and the CubeSats, computed via the ISL ranging measurements, brings a very high information content on the dynamics of the system, thanks to the closer distance of the CubeSats from the asteroids' center of mass (Gramigna et al. 2024b).

To this end, the precise trajectory reconstruction of Hera, Juventas, and Milani will allow estimating the low-degree and order gravity fields of Didymos and Dimorphos. When combined with the derived shape of both bodies, density inhomogeneities within these bodies could be constrained. Another byproduct of the Hera orbit determination is the estimation of the Didymos system's heliocentric trajectory, relying on a combination of ground-based astrometry (i.e., optical, radar, and stellar occultations), space-based astrometry from Hera images, and Hera range and ΔDOR measurements. An accurate ephemeris reconstruction is tightly linked to the estimation of the DART's heliocentric momentum enhancement factor $\beta_\odot$, representing an opportunistic science goal for the mission. Through these investigations, the Hera RSE will strongly contribute to asteroid science, being the first RSE investigation of a binary asteroid system and completing the planetary defence post-impact survey of DART.

2.1 Momentum Transfer

An accurate estimation of the mass of Dimorphos allows to determine the momentum transfer efficiency from the DART impact, which is defined through the momentum enhancement factor, β, and represents one of the most crucial parameters for planetary defense, see Fig. 3.

The β factor is defined as the ratio of the true system momentum change to the momentum change caused by an inelastic impact (Meyer et al. 2023; Feldhacker et al. 2017), namely:

$$\Delta\vec{v} = \frac{M_{\text{DART}}}{M_{\text{Dimorphos}}}\left[\vec{u} + (\beta - 1)(\hat{n}\cdot\vec{u})\hat{n}\right], \tag{1}$$

where M_{DART} is the DART spacecraft mass, $\vec{u}$ is the impact velocity vector, and $\hat{n}$ is the outward surface normal at the impact site.

Hence, the estimation of Dimorphos' mass and the constraints on its surface and interior structure, enabled by the Hera RSE, will allow us to assess the momentum transfer efficiency (characterized by the parameter β in Equation (1)) of the DART impact. For now, β is estimated to be between about 2 and 5 based solely on DART data (Cheng et al. 2023). An improved estimate of β from the DART impact, coupled with an extended knowledge

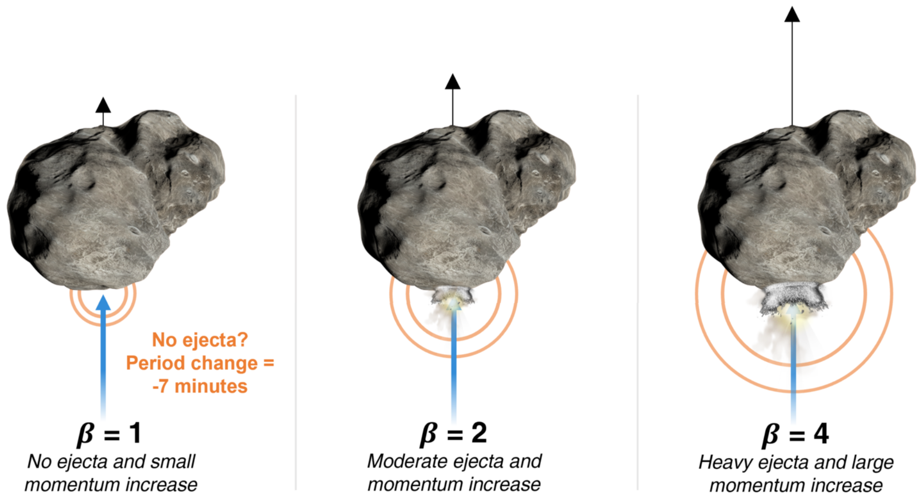

Fig. 3 Relation between the β factor, which depends on the mass of Dimorphos, relating Dimorphos momentum after the impact with DART momentum before the impact, and accounting for the momentum of ejected debris if any

about the geophysical properties of Dimorphos, will also potentially help in understanding the scaling of the momentum transfer efficiency to different asteroids for other missions and targets in the future.

Another relevant factor for characterizing DART's impact is the $\beta_\odot$ parameter, which represents the heliocentric momentum enhancement of the Didymos-Dimorphos binary system as a whole. The value of $\beta_\odot$ is expected to be smaller than β, depending only on the portion of ejecta that escaped the system. Detectable changes in the orbit will occur on longer time scales than those related to the mutual orbit period and have a similar magnitude to those induced by non-gravitational forces such as the Yarkovsky effect, making it harder to decorrelate these effects. Previous attempts to estimate $\beta_\odot$ using ground-based astrometry and stellar occultations to date have been unsuccessful (Makadia et al. 2022), primarily due to the limited time coverage of these high-accuracy measurements, which closely followed DART's impact. Combining pre- and post-DART ground-based astrometry with high-accuracy radiometric data from Hera's proximity operations will enable estimating $\beta_\odot$, provided a sufficiently high-fidelity model is used for Didymos' non-gravitational forces.

2.2 Geophysical Parameters

The Hera RSE will provide valuable insights into the geophysical characteristics of the bodies, mainly through the estimation of the Didymos system's gravity field but also through that of its rotational state. For example, the principal moments of inertia (MOI) can be recovered from the RSE, providing important constraints on the interior structure of the bodies for characterizing their radial internal mass distribution.

Within this investigation we can adopt two different methods depending on the actual dynamical state of the asteroids. The first one (the classical one), is based on the estimation of the Didymos system's gravity field through Stokes coefficients, and can be used if the system is found in a relaxed or non-chaotic dynamical state. The second one is an alternative approach using the Full Two-Body Problem (F2BP) formulation, which can also be used in case the system is in a chaotic or tumbling state. This latter method has several advantages both mathematical and numerical as it allows for a direct estimation of the moments of inertia and takes directly into account all their correlations with the estimated parameters (see Sect. 7.1.2 for more details).

In the classical framework, the estimated gravity field coefficients of Didymos and Dimorphos are used to return to the internal distribution of mass within these asteroids. If only degree-2 can be determined from RSE with statistical significance, then one can only infer the MOI and heterogeneity at the scale of half of the body radius, which is actually what is expected for Dimorphos (Gramigna et al. 2024b). In this case, the measured C_{20} and C_{22} will be combined with the measured libration amplitude of Dimorphos (w_a) to separately retrieve its principal MOI ($I_{XX} < I_{YY} < I_{ZZ}$). With perfect measurements and assuming $w_a \neq 0$ (which for non-zero orbital eccentricity also implies $C_{22} \neq 0$), the MOI can be computed as:

$$
\begin{aligned}
\frac{I_{ZZ}}{MR^2} &= 12C_{22}\left(1 - \frac{2e}{w_a}\right), \\
\frac{I_{XX}}{MR^2} &= 12C_{22}\left(1 - \frac{2e}{w_a}\right) + C_{20} - 2C_{22}, \\
\frac{I_{YY}}{MR^2} &= 12C_{22}\left(1 - \frac{2e}{w_a}\right) + C_{20} + 2C_{22},
\end{aligned}
\tag{2}
$$

where e is the orbital eccentricity and M and R the mass and radius of the body, respectively. In practice, however, Equation (2) should be replaced by a more general inversion which takes into account the uncertainties and correlations associated with the observed quantities. Such coarse constraints on the mass distribution inside the secondary asteroid may proven to be useful since large blocks within the interior of Didymos have been proposed to explain its non-circular equatorial perimeter (Barnouin et al. 2024), similarly to what is assumed for Bennu (Zhang et al. 2022). However, if the body is in a highly tumbling state, free libration modes could become excited. The resulting mixing of their amplitudes with forced libration modes would prevent us from accurately deducing the MOI as previously described. In this scenario, we note that we could still constrain the internal mass distribution by determining the natural frequencies. Alternatively, if Dimorphos is found to be in an excited, chaotic, or tumbling state, as predicted by Pravec et al. (2024), the second, F2BP-based, method may be more efficient. It allows for a direct estimation of both the moments of inertia and the rotational state. Details on the F2BP model can be found in Sect. 7.1.2.

For Didymos, a recovery of degree-4 gravity coefficients is expected by Hera RSE (Gramigna et al. 2024b). Using suitable inversion methods (e.g. Tricarico 2013 or Caldiero and Le Maistre 2024), this should allow us to constrain smaller-scale features, with a resolution relative to the volume scaling roughly as $1/l^2_{\max}$, although the sensitivity of these terms degrades rapidly with the depth. Direct inversion of these geophysical observables still represents an ill-posed problem. As done for rubble-pile Bennu, mitigation of the non-uniqueness of the interior estimation could come from targeting specific models (Scheeres et al. 2020) or fitting statistical distributions describing the size of the rubble-pile elements (Tricarico et al. 2021). Note that the large size of the boulders present on the binary asteroid surface (Pajola et al. 2024) hints at the two bodies having a rubble pile structure. For Dimorphos, surface features such as lineaments and troughs could suggest a stronger interior for the body, composed of elements that are more tightly packed compared to the unconsolidated surface (Barnouin et al. 2024). Analysis of the Hera RSE data should allow us to confirm or refute these theories on the internal structure of the Didymos system.

3 Observations

This section outlines how the Hera radio science measurements are derived from various observations. As shown in Fig. 4, the Hera mission involves several distinct observables. In the context of orbiting low-gravity bodies, traditional Earth-based Doppler measurements, typically the primary observable in interplanetary orbit determination, offer limited information. Therefore, a combination of different measurements is necessary to accurately estimate the scientific parameters of interest.

3.1 Observational Techniques

Measuring gravity in space requires assessing the relative acceleration between two objects. In planetary geodesy, this typically involves a spacecraft acting as a mass freely falling under the combined gravitational influence of a planet and other bodies in the solar system, with a ground-based antenna serving as a reference point. The exchange of radio signals between the spacecraft and the ground antenna enables the collection of radiometric data, including range, range rate, and angular measurements. These data are then integrated into a dynamic model of the solar system to derive various parameters related to solar system dynamics, gravity, planetary geodesy, and the study of planetary atmospheres and ionospheres.

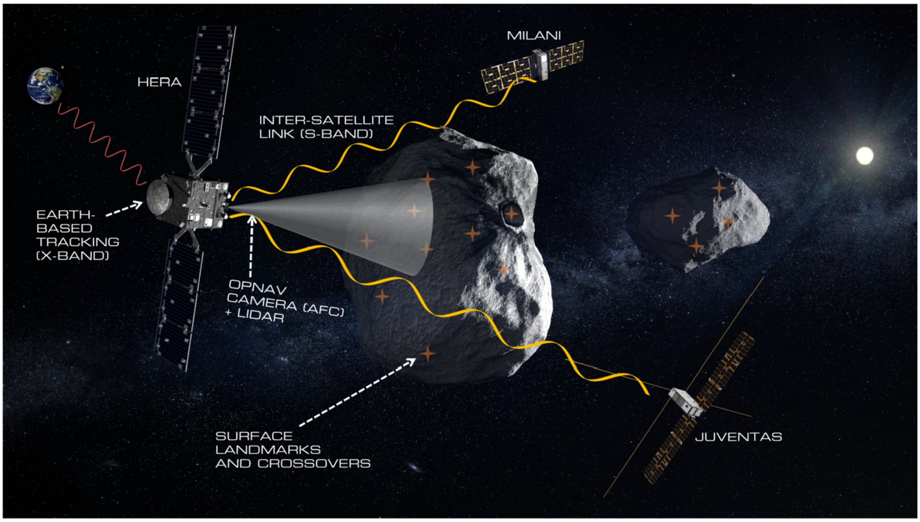

Fig. 4 Hera radio science experiment observational model. The observations included within the expected nominal Hera orbit determination are ground-based radiometric measurements, Hera optical images, Hera to CubeSats Inter-Satellite Link ranging measurements, and Hera LIDAR measurements to surface landmarks and crossovers on Didymos and Dimorphos. Some additional observables are expected to be employed in the orbit determination process, too, such as CubeSats optical images, Juventas' laser altimeter, GRASS gravimeter and JuRa radar, as well as optical information coming from Hera's Thermal Infrared Imager (TIRI) and Hyperscout hyperspectral imager cameras

Microwave links used in spacecraft tracking provide several observable metrics essential for navigation and orbit determination. The Hera RSE mission leverages multiple observations to gain a comprehensive understanding of the Didymos and Dimorphos asteroids. These include Earth-based range and range rate data, Delta-Differential One-way Ranging (Delta-DOR) observations, which help refine the orbital inclination of Didymos, as well as Inter-Satellite Link ranging measurements, optical images, and laser altimeter data.

3.1.1 Radiometric Tracking

Hera communicates with ground-based radio antennas, enabling the measurement of both range and range-rate between the spacecraft and Earth.

Two-Way Range-Rate Range-rate measurements correspond to the rate of change, in time, of the radial distance between the ground station and the spacecraft. Usually, the range-rate is accurately measured by exploiting the Doppler shift due to the relative motion between the two entities. Let's assume that at time t_1 the ground station transmits a stable frequency carrier $f_T(t_1)$. The onboard transponder then receives this signal and generates a cleaned, coherent copy using a Phase-Locked Loop (PLL), with a frequency f'_R at time t_2 (different from f_T due to the relativistic Doppler effect, dispersive and non-dispersive media noise, etc). To prevent interference between incoming and outgoing signals, the copied signal is multiplied by a pre-determined Turn Around Ratio (TAR) and re-transmitted back (phase-coherently) with a frequency $f'_T = \text{TAR}\ f'_R$.

As a first-order approximation, the received frequency at the ground station (or receiving spacecraft) at time t_3 is then:

$$f_R(t_3) \simeq \text{TAR}\ f_T(t_1)\left(1 - \frac{\dot{r}_{12} + \dot{r}_{23}}{c}\right), \tag{3}$$

where $\dot{r}$ are the one-way range-rate, while $\dot{\rho} = \dot{r}_{12} + \dot{r}_{23}$ is the two-way range-rate.

Therefore, knowing $f_R(t_3)$, $f_T(t_1)$ and the TAR, one can evaluate the range-rate exploiting the Doppler shift:

$$\frac{f_R(t_3) - \text{TAR}\ f_T(t_1)}{\text{TAR}\ f_T(t_1)} \simeq -\frac{\dot{\rho}}{c}. \tag{4}$$

From a practical point of view, a Doppler counter precisely measures the overall phase change within a specified count time, denoted as T_c, and the Doppler shift is evaluated using Equation (5) (Buccino et al. 2022; Moyer 2005).

$$f_{\text{Doppler}} = \frac{\phi\left(t + \frac{T_c}{2}\right) - \phi\left(t - \frac{T_c}{2}\right)}{2\pi \cdot T_c}, \tag{5}$$

where f_{Doppler} is the range-rate observable, ϕ is the received radio signal phase of the residual carrier, T_c is the count time. Each time the phase of the received signal undergoes a shift of one cycle compared to the phase of the transmitted signal, the distance covered by the signal increases by one wavelength, equivalent to 3.6 cm at X-band. Consequently, the Doppler count offers a quantification of the change in range over the duration T_c (Thornton and Border 2003).

This setup, typical for closed-loop receivers, is particularly effective for near-real-time measurements, although it is not always ideal for high-precision measurements. Alternatively, the observed data can be derived from the phases obtained through a wideband sampling of the received signal, following appropriate downconversion. These recorded carrier samples are subsequently processed using a fully digital phase-locked loop, which enables precise reconstruction of the received signal's phase, frequency, and amplitude. This open-loop method offers several benefits, including greater flexibility in adapting the PLL to varying noise conditions (which reduces noise at short integration times), increased resilience to noise effects, and improved capability for identifying instrumental issues.

Two-Way Range Two-way range measurements are employed for both the direct to Earth link (between Hera and Earth) and the ISL between CubeSats and Hera.

For the Earth link, the range observables measure the linear distance between the spacecraft and Earth and are derived by measuring the time delay between the transmission and reception of a known signal (ranging signal) modulated on the carrier signal. In a coherent two-way configuration, the ground station sends a modulated ranging signal on the uplink carrier, which is then received and locked through a PLL by the spacecraft then relayed back and received again by the ground station. The onboard transponder either regenerates and remodulates the uplink ranging signal onto the downlink carrier (regenerative ranging) or simply retransmits the ranging signal without code acquisition (transparent ranging). The Round-Trip Light Time (RTLT) of this process represents the range measurement. Both the traditional sequential ranging method (ECSS 2008) and the modern PN (pseudo-noise) ranging method (CCSDS 2014) are supported by NASA and ESA ground stations. One of the main issues, due to the periodic nature of the ranging signal, is the phase ambiguity, which can be resolved using the known a priori position of the spacecraft. The measurement's accuracy is inversely proportional to the ranging clock component of the signal, meaning higher frequencies lead to better precision.

For CubeSat-to-Hera range measurements,, Hera communicates with the two companion CubeSats by means of an ISL radio system. The same ISL unit is present on board all the spacecraft and forms the range observables to enable the CubeSats navigation and radio science. The ranging measurements are performed between a pair of nodes directly connected through exchange of packets, using a round trip time technique, see Sect. 4.2.

Delta-DOR Delta-DOR is a tracking measurement based on the principle of very-large baseline interferometry, which consists of measuring the time difference in the reception of a radio signal transmitted by the spacecraft at two widely separated ground stations. This time difference provides information on the spacecraft plane of the sky position with respect to the baseline vector between the stations, complementing the line of sight information provided by the range and Doppler data. Delta-DOR measurements are typically used to improve the orbit determination accuracy in preparation for critical mission phases such as planetary flybys, or deep space and orbit injection maneuvers, and have been used in support of ESA deep space missions since 2006 (Iess et al. 2006; James et al. 2009; Barbaglio et al. 2012; Fiori et al. 2022).

In addition to ESA's standard narrowband capabilities, Hera will demonstrate a novel Wideband Delta-DOR (WBDDOR) technique based on spread-spectrum waveforms, which is expected to improve the measurement precision to less than 1 nrad, thanks to an updated X-band Deep Space Transponder (Cardarilli et al. 2019). The potential to improve the orbit determination accuracy in proximity to the Didymos system will be a key enabling factor for the estimation of non-gravitational accelerations and torques acting on the system, and to decouple these effects from the heliocentric momentum enhancement $\beta_{\odot}$ from DART's impact.

3.1.2 Optical Observations

Radiometric measurements are supplemented by optical observations from the spacecraft's navigation cameras. Hera is equipped with two identical Asteroid Framing Cameras (AFC) developed by JenaOptronik, whose design is based on the Astrohead cameras. The cameras have an array size of 1020 × 1020 pixels with a field of view of 5.5 × 5.5 deg and an Instantaneous Field of View (IFOV) of 94.1 μrad. Juventas and Milani navigation cameras are used primarily for navigation purposes but will also be used to perform scientific investigations. Juventas NavCam is a 58 × 36 × 33 mm visible imager with a resolution of 2048 × 1536 pixel, and a Field Of View (FOV) of 38.0 × 28.5 deg; Milani optical imager has a resolution of 2048 × 1536 pixel and a FOV of 21 × 16 deg (Ferrari et al. 2026).

Due to the relatively small velocities and accelerations near the Didymos system, traditional Earth-based Doppler measurements, typically used as the primary observable in interplanetary orbit determination, provide limited information. Therefore, spacecraft navigation must be enhanced through additional observations, such as ISL radiometric and optical measurements from onboard cameras, which help constrain the spacecraft's relative position with respect to the asteroid system.

When targeting a distant object, an image of the body provides its relative direction with respect to the spacecraft in the camera's frame (centroid). At closer range, the camera can identify surface features (landmarks), which allow for a more accurate estimation of the body's rotational state. Specifically, recognizing surface landmarks on both Didymos and Dimorphos during the Orbit Determination (OD) process is crucial for establishing control points and precisely triangulating the spacecraft's position. Additionally, in a binary system like Didymos, optical measurements also provide the accurate relative positions of the two bodies, imposing a strong constraint on their relative orbital motion.

The relative orbital motion reveals information about the system's total mass, and if this motion is measured with respect to the common center of mass, which is inertially fixed, the mass ratio of the two bodies can also be determined. The inertial motion of the secondary primarily provides data on the mass of the primary, and vice versa. However, optical measurements are influenced by scaling symmetry, as they do not directly provide information on the relative distance to a body: the same optical observations can be reproduced by changing both the spacecraft-body distance and the body size by the same scale factor, S. This scaling symmetry also affects mass estimation: under the two-body approximation, the same series of images can be generated by adjusting the body mass by S^3. In a binary system, the scaling symmetry applies similarly, as the same optical measurements can be obtained by also altering the primary-secondary distance by the same scale factor (Zannoni et al. 2018). This scaling symmetry can be constrained using a priori information about the estimated parameters and by incorporating different observables, such as Doppler and range measurements, which provide absolute velocity and distance data relative to Earth.

3.1.3 Laser Altimeter

In laser altimetry measurements, employed by planetary altimeters, the spacecraft directs the laser beam directly toward the nadir and measures the two-way time of flight. Laser altimetry measurements contribute to a more precise reconstruction of the spacecraft trajectory, enabling their integration with radiometric and optical observables to enhance the estimation of the gravity field for both celestial bodies and their relative orbits, as demonstrated by Hayabusa, MESSENGER (Tsuno et al. 2017), Lunar Reconnaissance Orbiter (LRO) (Ramos-Izquierdo et al. 2005, 2009), Hayabusa2 (Mizuno et al. 2017), and OSIRIS-REx (Daly et al. 2017).

Within the OD process, the altimetry observables can be treated as a standard range measurement, namely:

$$\rho = \sqrt{(\vec{r_1} - \vec{r_2})^T (\vec{r_1} - \vec{r_2})}, \tag{6}$$

where 1 is the spacecraft, 2 the target (a surface landmark or crossover), and $\vec{r_i}$ the position vector of the i relative to the center body in the inertial coordinate frame, where i can be either 1 or 2.

Furthermore, a crucial element in improving orbit reconstruction is the estimation of a set of LIDAR crossovers. These crossovers, defined as surface landmarks probed multiple times by different LIDAR swaths, have been extensively utilized in the past to refine the orbital determination solutions derived from radiometric and optical data (Rowlands et al. 1999; Lemoine et al. 2001; Mazarico et al. 2010, 2014, 2015). In particular, they allow for the cancellation of a major source of error in this data, namely, the uncertainty in the topographic elevation profile and shape of the target body. Indeed, the estimation of crossovers within the OD process allows to constrain their initial position uncertainty on the surface, which is mainly driven by the asteroids' shape uncertainty. Knowing that the asteroid radius is constant at ground-track intersections (with only minor deformations caused by tides), these measurements serve as valuable constraints for determining and constraining the spacecraft's orbit, resulting in a more accurate reconstruction of Hera's position relative to the asteroid. Hera measures its altimetry with respect to a surface landmark (called crossover) at different orbits, obtaining the measurements $r(t)$. Hence, Hera's position relative to the asteroid at time t_1 is:

$$\vec{O}_1(t_1) = \vec{r}_1(t_1) + \vec{h}_{CXO-1} + \vec{\Delta} h_{CXO-1}, \tag{7}$$

where $\vec{h}_{CXO-1}$ is the crossover #1 position on the asteroid surface and $\vec{\Delta} h_{CXO-1}$ is its position uncertainty due to the shape uncertainty.

The same can be obtained from a measurement of the same crossover #1 obtained at a different orbit at time t_2:

$$\vec{O}_2(t_2) = \vec{r}_2(t_2) + \vec{h}_{CXO-1} + \vec{\Delta} h_{CXO-1}. \tag{8}$$

Combining the two observables we can build the LIDAR constraint:

$$\vec{O}_2(t_2) - \vec{O}_1(t_1) = \vec{r}_2(t_2) - \vec{r}_1(t_1), \tag{9}$$

where we can observe that the shape uncertainty cancels out, and the constraint between Hera's two orbits becomes proportional to the altimetry measurements, with the remaining uncertainty depending solely on the instrument's performance. Figure 5 shows a visual representation of this concept.

It is worth noting that, in order to properly exploit LIDAR crossovers with high accuracy, it is essential to determine the exact location of the LIDAR footprint on the surface. This requires accurate pointing calibration of the altimeter relative to the spacecraft and co-registration with optical imagery. In the Hera mission, the LIDAR instrument will be calibrated in combination with the AFC cameras, following standard procedures similar to those adopted in previous missions (e.g., alignment of the Hayabusa2 laser altimeter relative to its optical navigation camera (Noda et al. 2021)). This joint calibration ensures that each altimetric return can be associated with a precisely identified surface landmark in AFC images, thereby enhancing the robustness of crossover determination. Nevertheless, residual co-registration errors—stemming from alignment uncertainties, parallax effects, or thermal instabilities—may still limit the achievable accuracy of the method.

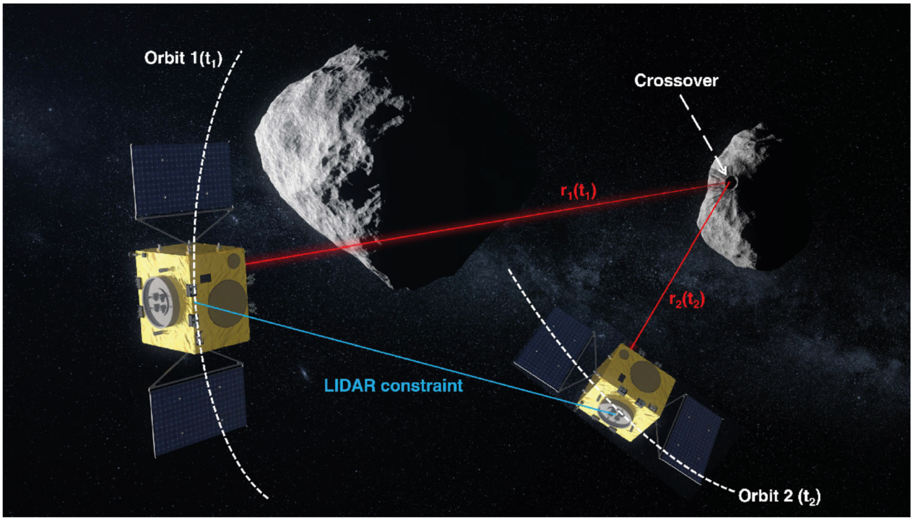

Fig. 5 Visual representation of the LIDAR and crossovers constraints on Hera's orbits

3.1.4 Other Observations

Other observables are expected to be used within the Hera RSE to further improve the orbit determination process. Among them, the CubeSats optical images obtained by Juventas and Milani navigation cameras, Juventas' laser altimeter, GRASS gravimeter and JuRa radar, star trackers on board the CubeSats after the landing to reconstruct the asteroid's attitude, as well as optical information coming from Hera's Thermal Infrared Imager (TIRI) and Hyperscout hyperspectral imager cameras.

4 Hera Radio System

4.1 Direct to Earth

4.1.1 X-Band Deep Space Transponder

The Earth-based two-way radiometric Doppler and range measurements are performed exploiting Hera's X-Band link Deep Space Transponder (X-DST) developed by Thales Alenia Space Italia (TAS-I), which will allow for simultaneous transmission of housekeeping telemetry data and receiving telecommands from the ground, see Fig. 6. The system is derived from a modular platform designed, developed, and qualified in the frame of previous deep space programs such as ExoMars 2016 (in-flight), ExoMars 2020, SolarOrbiter (in-flight), and Juice DST (in-flight).

The main X-DST receiving functions are summarized in Table 2. Furthermore, this system will support standard Delta-DOR tracking from Earth ground stations, and it will be the first mission to carry out an in-flight characterization and demonstration of the novel WBDDOR performances.

Finally, in terms of performances, the X-DST end-to-end Allan standard deviation (Riley 2008) is $8 \cdot 10^{-15}$ at 60 s integration time ($2 \cdot 10^{-15}$ at 1000 s integration time).

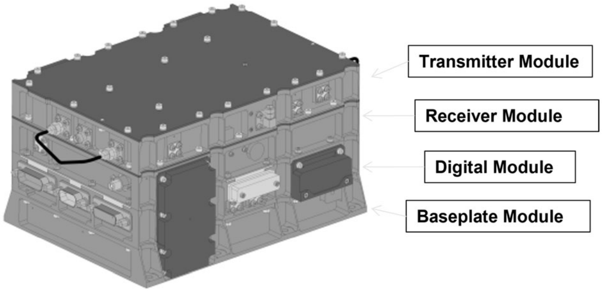

Fig. 6 Hera X-DST transponder developed by Thales Alenia Space Italia

Table 2 X-DST receiving and transmitting main functions

Receiving Functions	Transmitting Functions
– Acquisition and tracking of the up-link carrier	– Data modulation according to the specified signalling schemes
– Tracking and demodulation of data from a 16 kHz subcarrier in BPSK/NRZ format	– Downlink carrier modulation with ranging and/or modulated telemetry
– Command data decisions and recovering of the bit timing for the system management unit	– Non-coherent capability whereby the down-link frequency is derived within the X-DST to provide a fixed transmit frequency telemetries
– Standard ranging demodulation and automatic gain control	– Coherent capability whereby the down-link frequency is related to the received frequency through the 880/749 turn-around ratio
– Pseudo-noise ranging on-board regeneration	– Delta-DOR and WBDDOR modulation

4.1.2 The Ground System

Earth-based radiometric radio science observables are generated at ground stations that are part of the ESA ground network (ESTRACK) and NASA Deep Space Network (DSN). These networks consist of strategically positioned complexes around the globe, equipped with large-aperture antennas ranging from 34 to 70 meters in diameter, ensuring near-continuous communication with spacecraft throughout the solar system. Figure 7 shows the ESA Deep Space Antenna (DSA) in Malargüe, Argentina.

Each station is equipped with an exciter-transmitter system to support uplink communication and a front-end microwave subsystem that provides low-noise amplification and initial down-conversion of radio signals. The radio signals are also recorded for subsequent analysis, by mixing them to lower frequencies. In addition, two-way and three-way uplink transmissions provided by the networks are modulated with ranging codes, which enable the determination of the distance between the two elements by correlating it with the modulated downlink signal, as explained in Sect. 3.1.1.

Precision Doppler tracking of Hera is performed using a two-way link, where signals are transmitted from the ground to the spacecraft and then phase-coherently retransmitted back to the same ground antenna. A highly stable frequency standard, such as a hydrogen maser, provides the reference for both transmission and reception. The X-band uplink is coherently retransmitted to Earth on an X-band downlink using the Hera X-DST transponder.

Radio science data are acquired using two types of receivers: closed-loop and open-loop. The closed-loop receiver employs a phase-locked loop (PLL) to track the spacecraft signal carrier precisely, measuring and recording the carrier's phase. The Doppler shift can be

Fig. 7 ESA's Malargüe deep space ground station. Image credit: ESA/Filippo Concaro

estimated from this phase data and converted into relative radial velocity (see Sect. 3.1.1, in particular Equations (4)–(5)). The closed-loop tracking receiver guarantees carrier phase and range data at a rate determined by the code repetition period and user-selected averaging interval.

In contrast, open-loop reception uses an independent broadband receiver without the phase-lock loop tracking mechanism. Instead, the receiver down-converts the spacecraft signal via a local oscillator heterodyne process, guided by a prediction of the expected frequency.

4.1.3 Media Calibrations

The radiometric measurements received on Earth are affected by several error sources caused by environmental interactions that must be calibrated to accurately determine the physical parameters of interest. These include dispersive noises, such as the charged particles within the solar plasma and the Earth's ionosphere, and non-dispersive noise sources, like the Earth's troposphere. DSN and ESTRACK tracking stations used by the Hera mission routinely produce GNSS-based calibrations to remove the low-frequency radiometric errors induced by the Earth's ionosphere and troposphere (Feltens et al. 2018). Furthermore, ESTRACK's DSA-3 antenna in Malargue (ARG) and DSN's DSS-25 complex in Goldstone (CA) are endowed with calibration systems to correct for the high-frequency Doppler noise induced by path delay variations in the Earth's troposphere. The two calibration systems, respectively called Advanced Water Vapor Radiometer (AWVR) (Buccino et al. 2021) and Tropospheric Delay Calibration System (TDCS) (Lasagni Manghi et al. 2021, 2023), are expected to provide Doppler data of excellent quality. The dispersive noise induced by charged particles in the interplanetary plasma and solar corona cannot be removed from Hera data since the spacecraft is not equipped with a multi-frequency link. Therefore, accurate modeling of such effects should be introduced.

4.2 Inter-Satellite Link

Hera communicates with the two companion CubeSats by means of an ISL radio system. The CubeSats rely on Hera to relay their data and commands to and from the operation centers on the ground. The ISL allows their correct communication and data relay (e.g., telecommands, housekeeping data, telemetry, and payload data), and it forms the observables to enable the CubeSats navigation and radio science (Gramigna et al. 2022).

The ISL is based on a spread spectrum signal in the 2.4 GHz S-band (Proba-3 concept), see Figs. 8–9. The system provides ranging based on subsample accuracy time of flight with an Oven Controlled Crystal Oscillator (OCXO) as the reference clock. The ranging measurements are performed between a pair of nodes directly connected through the exchange of packets, using a round trip time technique. Figure 10 depicts one instance or cycle of the ISL implementation of the link state packets exchange. In each cycle, three packets are exchanged, allowing for both nodes to estimate the link quality, the distance, and the clock offset between nodes.

The initiation node, identified as node A in Fig. 10, issues the first packet in the network. In response, node B, upon receiving the first packet, calculates the time difference between its reception and the transmission of the second packet. Node A, upon receiving the second packet, compares the time difference between the reception of the second packet and the transmission of the first packet with the reported time difference in the second packet. This process allows for the computation of the distance between nodes. The third packet provides similar information for node B. Each packet's time duration is on the order of a few milliseconds, with a time interval of approximately 20 milliseconds between two packets. The original concept depicted in Fig. 10 from the Tekever ISL has been improved to a 4 packet exchange process as part of the Hera development, allowing both ISL nodes to perform same estimations.

Furthermore, clock synchronization is meticulously maintained among all relevant devices in each transceiver, and the transmission and reception of each packet are synchronized by a clock-conscious Field Programmable Gate Array (FPGA), ensuring precise transmission instants. The modulation employed enables the determination of the reception instant of each packet with subsample accuracy. Clock offset estimation, crucial for ranging accuracy, considers both the natural offset between the independent clock sources of the two nodes (OCXO devices) and the Doppler effect resulting from potential relative motion. This clock offset is measured from the synchronization preamble transmitted at the beginning of each packet, lasting about 360 microseconds.

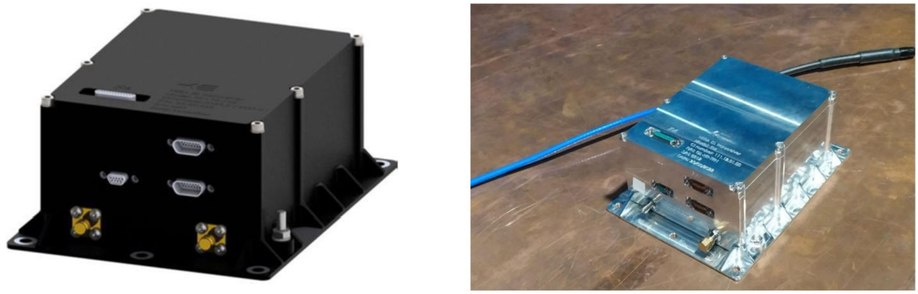

Fig. 8 Tekever ISL unit for Hera

Fig. 9 Tekever ISL unit for the CubeSats

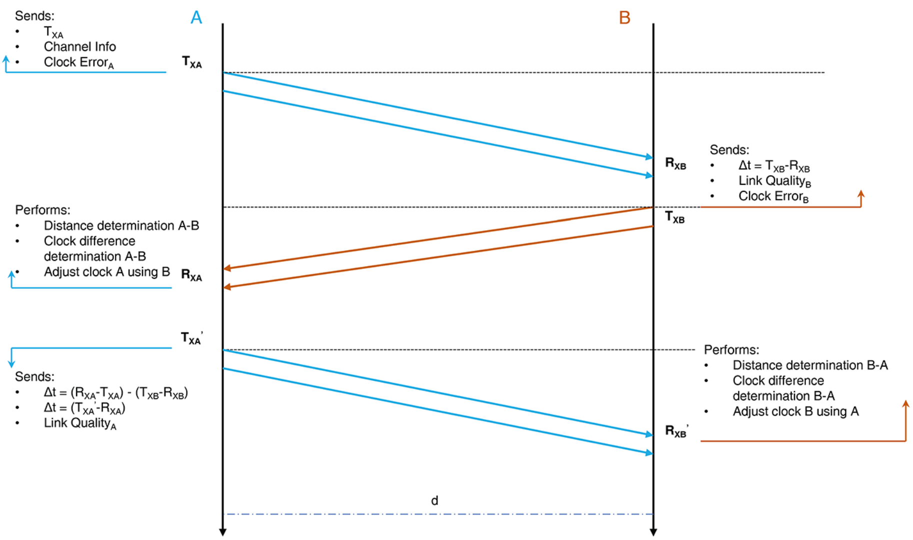

Fig. 10 Tekever ISL ranging architecture

Table 3 ISL Bit depth

Duration	MegaByte (MB)
1 day	1.4
1 week	9.7
1 month	38.7
2 months	77.4
3 months	116.1

A dedicated radio science ranging mode within the ISL unit has been developed, too. In particular this mode allow to increase the rate of measurements up to 5 sample per seconds (with reduction of data exchanged in parallel). In addition, the same observables are available at both ends of the link.

Finally, we quantify the expected sample rate and data volume of the ISL unit, relevant for Hera's data budget and operations planning. We assume:

- 1 sample per second for both range and time-stamp;
- 100% duty cycle (worst case);
- 3 months of operation (nominal CubeSat mission).

Each sample consists of two double-precision values (range and time-stamp), i.e., 2 × 64 bit = 128 bit = 16 byte per sample per CubeSat. The resulting conservative upper-bound data volume is summarized in Table 3.

5 Error Budget

5.1 Radiometric Tracking

5.1.1 Direct to Earth

The main noise factors that affect the Earth-based radio science observables are the solar, interplanetary, and ionospheric plasma, the S/C electronics, the ground station instrumentation, the Earth's troposphere, and thermal noise. Thermal noise is particularly significant at short integration times (1–10 s), but becomes negligible compared to the other contributions at longer integration intervals, such as the 60 s typically used for range-rate measurements in gravity science experiments. Hera X-DST performances correspond to a Doppler error contribution of 2.4 µm/s at 60 s integration time (0.6 µm/s at 1000 s). Regarding the other terms, the expected Earth-based Doppler noise level is quantified using empirical models of the primary noise sources (Asmar et al. 2005; Iess et al. 2014a).

Figure 11 shows the aforementioned expected noise sources for the Hera mission in terms of the Allan standard deviation as well as error introduced in the range-rate measurements and evaluated at 60 s integration time (typical integration time adopted in gravity science studies to balance numerical noise, computational burden, and sensitivity to gravity spherical harmonics (Zannoni and Tortora 2013; Gramigna et al. 2024b). The Doppler noise is dominated by the plasma noise, which slightly increases towards the end of the mission due to lower Sun-Earth-Probe (SEP) values.

Furthermore, the Earth-based range data is expected to be affected by errors in the order of 3.4 ns (100 cm) for the high-frequency noise, 3 ns (90 cm) for the calibration error, and 3 ns (90 cm) for aging and drift.

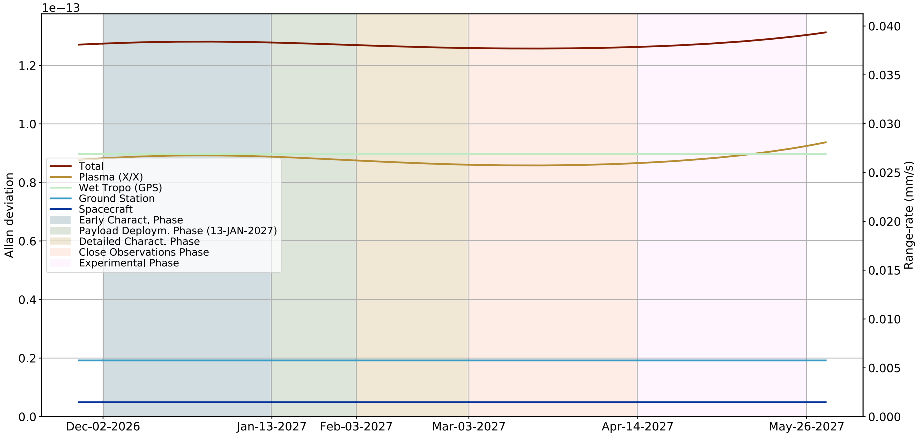

Fig. 11 Allan deviation and relative error introduced in the range-rate at 60 s integration time of the main noise sources for the Hera mission. The noise contributions of the ground stations, the Earth's troposphere, and the plasma are evaluated using the analytical models from Asmar et al. (2005), Iess et al. (2014a), with thermal noise already accounted for in the ground station and spacecraft curves. The plasma model incorporates the effects of both the interplanetary plasma and the ionospheric plasma. The Hera spacecraft noise reflects the X-DST performance stability tests conducted by TAS-I. The total curves are obtained as the root squared sum of the individual contributions. Notably, the primary noise sources are attributed to Earth's troposphere and plasma

5.1.2 ISL

ISL measurements, as opposed to standard Earth-based links, are not affected by the noise contributions due to the Earth's atmosphere and to the interplanetary plasma (which is negligible at short distances). As a result, the limiting factors are mainly the stability of ISL system electronics and their thermal noise.

The ISL ranging jitter noise was characterized through laboratory testing of the Hera ISL Proto Flight Model (PFM) and its associated Electrical Ground Support Equipment (EGSE) under steady-state conditions. The units were connected via cable, exchanging link state packets at a rate of one cycle per second. We performed an Allan deviation analysis on ranging data collected from an extensive series of measurements taken in a controlled environment. Preliminary results, presented in Fig. 12, show an Allan deviation dominated by white noise, with a characteristic slope of -0.5. The preliminary 1σ uncertainty for the ranging jitter is 3 cm.

It is worth noting that the range measurements are also subject to an overall range bias, which has not been characterized yet for the ISL system. The reported 3 cm jitter refers to short-term measurement fluctuations under laboratory conditions; in realistic operational scenarios, additional sources of error—including thermal noise, spacecraft electronics, and clock stability—are expected to increase the total range uncertainty. Although Doppler measurements are not natively provided by the ISL hardware, synthetic range-rate observables can be generated by differentiating range measurements to eliminate the range bias. Only one observable type—either raw range or synthetic range-rate, depending on the in-flight characterization of the range bias—will be ingested by the OD filter, avoiding any duplication of correlated measurements that cannot be treated as independent.

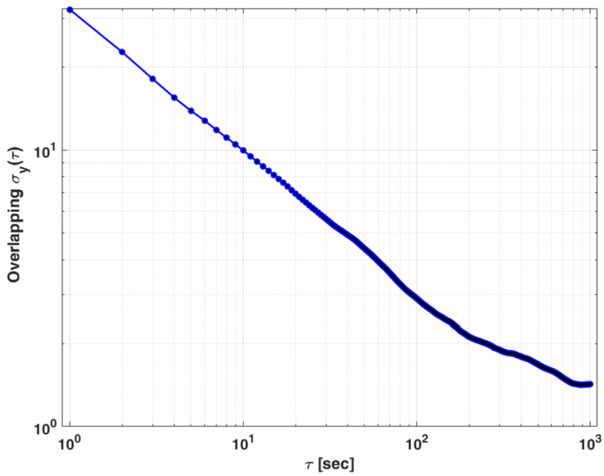

Fig. 12 Preliminary Allan deviation of ISL ranging data obtained from laboratory tests

5.2 Optical

Optical data accuracy is heavily influenced by several factors, including the precision of the reconstructed camera pointing, the overall imaging geometry, the image processing algorithms, and, crucially, the characteristics of landmark features. These features include their distance, solar illumination angles, and the frequency and number of observations. Previous missions to small bodies have achieved landmark optical residuals with an overall RMS (root mean square) on the order of 0.1–1 pixels in both sample and line directions (Konopliv et al. 2014, 2018; Godard et al. 2015; McCarthy et al. 2022). Similar performance is expected for Hera; however, the effectiveness of landmark matching depends on the presence of well-defined surface features. This may pose a challenge for Didymos, a fast rotator with a relatively smooth surface, in contrast to comet 67P/Churyumov-Gerasimenko, which has distinct features. Given this, we maintained a conservative approach in our simulations by incorporating a healthy margin and assuming a noise level of 2 pixels in both sample and line directions.

5.3 LIDAR

Hera is equipped with a Jenoptik Laser rangefinder module DLEM-45, which adopts a pulse accumulation principle at a wavelength of 1.55 μm, see Fig. 13. The LIDAR instrument presents a good performance until the range of around 20 km, with an expected overall range accuracy of about 1 m (1σ).

5.4 Delta-DOR

The Delta-DOR error budget depends on many systematic and random errors, including spacecraft and quasar thermal noises, dispersive phase, clock instability, propagation media errors (i.e. solar plasma, ionosphere, and troposphere), Earth orientation, and station and quasar coordinates. Analytical expressions for the individual error contributions can be found in the CCSDS technical report along with the assumptions used for their derivation (CCSDS 2013). Most of the systematic contributions can be directly modeled in the OD filter as solved-for or consider parameters. All the remaining contributions are then root-sum-squared to obtain the global error, which is currently estimated to be on the order of

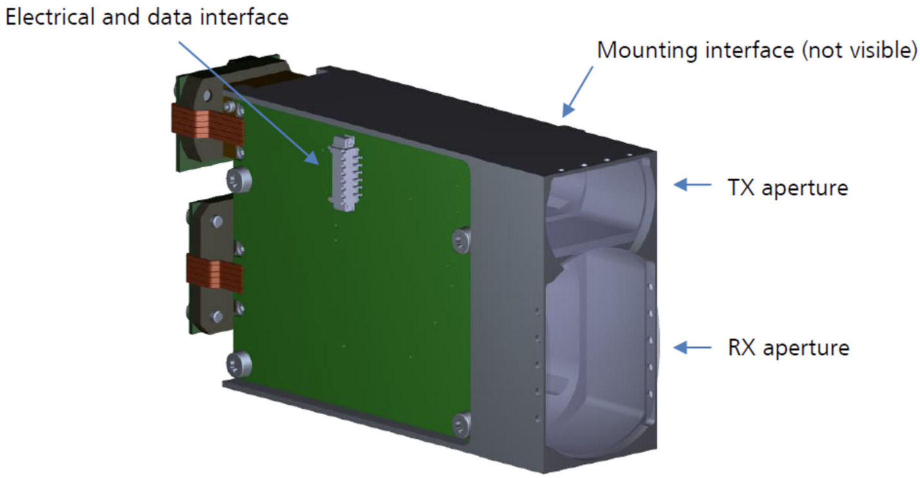

Fig. 13 Jenoptik laser rangefinder module functional elements. Image credit: Jenoptik

0.05 ns, which corresponds to 300–700 m once projected in the plane-of-sky direction at characteristic Hera distances. However, consolidating the error budget will only be possible once the ESOC Flight Dynamics team selects the actual quasars for the observations during operations. A slight reduction in Delta-DOR noise is also expected for the wide-band measurements, to be tested for the first time on an ESA mission during the Hera cruise phase.

6 Hera Operations and Data Acquisition

6.1 Cruise

Hera's cruise trajectory is reported in Fig. 14. The cruise will be used to calibrate the spacecraft's instruments and cameras and perform checkouts on the CubeSats payloads. Regarding the RSE, during the cruise, we plan to accurately reconstruct Hera's heliocentric trajectory from radiometric measurements (range, Doppler, Delta-DOR, WBDDOR). Furthermore, we are particularly interested in the Mars swing-by, which will be performed in March 2025, to provide estimates of Deimos and Phobos ephemeris exploiting AFC optical images and radiometric data, with the goal to constrain Hera absolute motion and Deimos relative motion.

The cruise will also be used to test the WBDDOR modulation of the X-DST, as well as to compare the a priori uncertainty (correlator) and RMS of residuals with conventional Delta-DOR. From the scientific point of view, the characterization of this new modulation is relevant for cruise and proximity operations (as it provides higher measurement accuracy) for an increased scientific return of parameters like heliocentric beta, $\beta_{\odot}$, and the Yarkowsky non-gravitational acceleration effect. Finally, Hera's arrival is expected at the end of November 2026, which will begin the asteroid nominal phase.

6.2 Asteroid Phase

The asteroid phase is composed of the following main phases (Gramigna et al. 2024b):

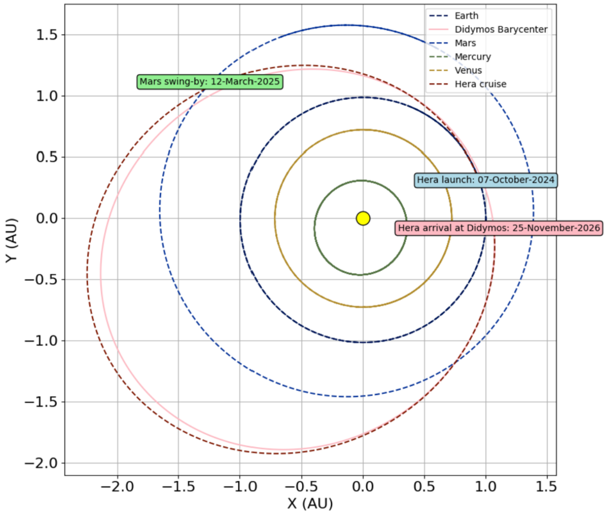

Fig. 14 Hera's Cruise Trajectory. Hera was launched on October 7, 2024. The mission includes a planned Mars flyby in March 2025, with arrival at the Didymos system scheduled for late 2026

- Early Characterization Phase (ECP, 6 weeks, starting on 02 December 2026): series of 3–4 days hyperbolic arcs, with distances between 20–30 km from the Didymos system. This phase is used for initial mapping and understanding of the targets, preparing the spacecraft and operations for the subsequent closer phases;
- Payload Deployment Phase (PDP, 2 weeks, starting on 13 January 2027): beginning of CubeSats release operations and commissioning;
- Detailed Characterization Phase (DCP, 4 weeks, starting on 03 February 2027): the trajectory is characterized by hyperbolic arcs at distances around 8–20 km from the Didymos system, similar to the ECP scheme. From this phase, the closer distance requires Hera to employ an autonomous attitude guidance, using centroiding information for Didymos (and potentially also Dimorphos) from onboard processing of the optical images for navigation. In this phase, dedicated ISL ranging measurements for scientific purposes also begin.
- Close Observation Phase (COP, 6 weeks, starting 03 March 2027): follows the same DCP scheme with closer flybys up to 4 km altitude. In this phase, fully autonomous attitude guidance is required, and below 8 km, the Hera AFC camera is expected to be pointed at Dimorphos. In terms of gravity science, this phase will provide high-resolution recovery of Didymos' extended gravity field, thanks to Juventas' low Self-Stabilized Terminator Orbit (SSTO). Within this phase, support for CubeSats' operations for their potential landing and disposal is also foreseen.
- Experimental Phase (EXP, 6 weeks, starting on 14 April 2027 and ending on 26 May 2027): lower flybys down to 1–2 km from Didymos and Dimorphos will be performed. Depending on the actual flybys performed, further improvements in the recovered asteroids main scientific parameters of interest could be obtained.

The trajectories of Hera, Juventas, and Milani are depicted in Figs. 15, 16, and 17, respectively. Hera and Milani's trajectories feature hyperbolic arcs, with an SSTO expected for Milani during the experimental phase, before starting landing operations. Juventas first enters a 3.3 km altitude SSTO, followed by a second SSTO at an altitude of 2.0 km, before beginning its landing approach to Dimorphos.

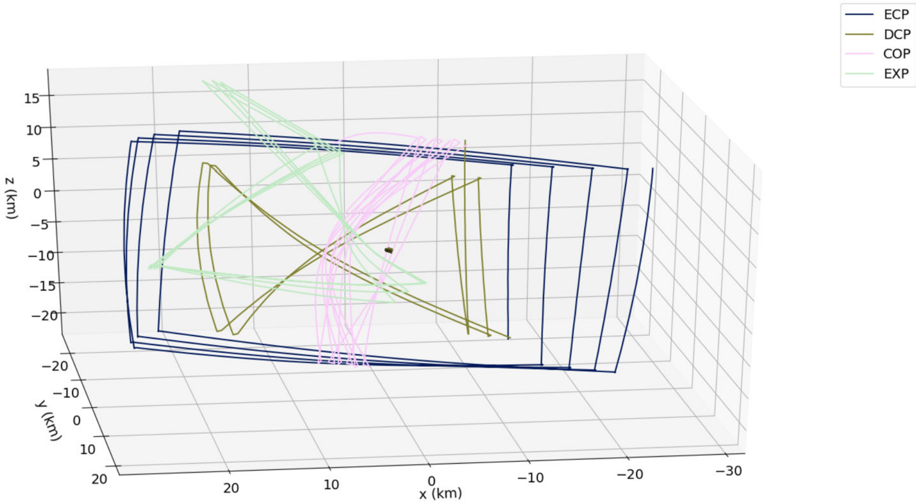

Fig. 15 Trajectory of Hera during the asteroid phase and extended phase. During the nominal mission, Hera follows a series of hyperbolic arcs lasting 3–4 days each, at distances ranging from 30 to 4 km from the Didymos system. In the extended phase, these distances decrease to as close as 1–2 km

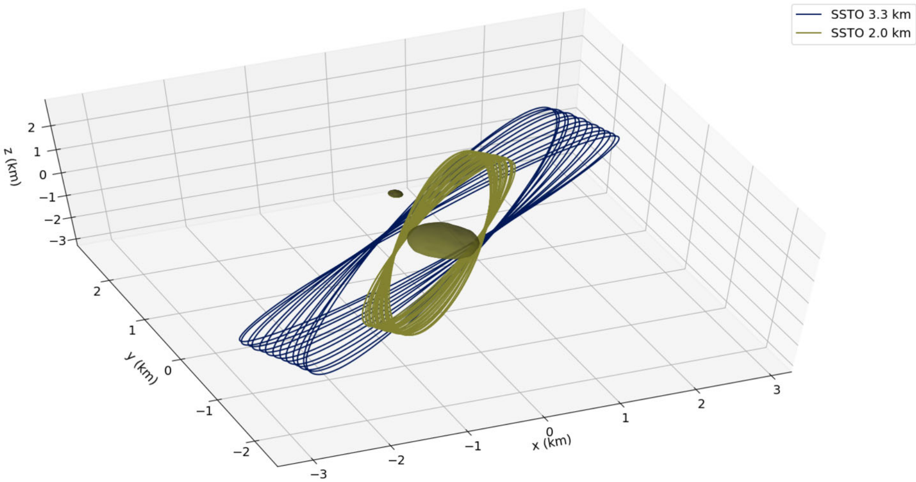

Fig. 16 Juventas SSTO orbits during the nominal asteroid phase. Following these orbits, Juventas is expected to land on Dimorphos

6.3 Data Acquisition

The expected RSE data acquisition during the asteroid phase is provided in Fig. 18. During the ECP, we assume to collect Earth-Hera two-way range and Doppler measurements at X-band for 4 h before and 4 h after each maneuver at the corners in between arcs, corresponding to a hyperbolic trajectory arc of Hera, and for 8 h around the Closest Approach (CA) to Didymos. Regarding the DCP-COP and EXP, Earth-based radio tracking is performed only at the beginning and end of each arc. During low-altitude flybys (i.e., below 8 km), the AFC

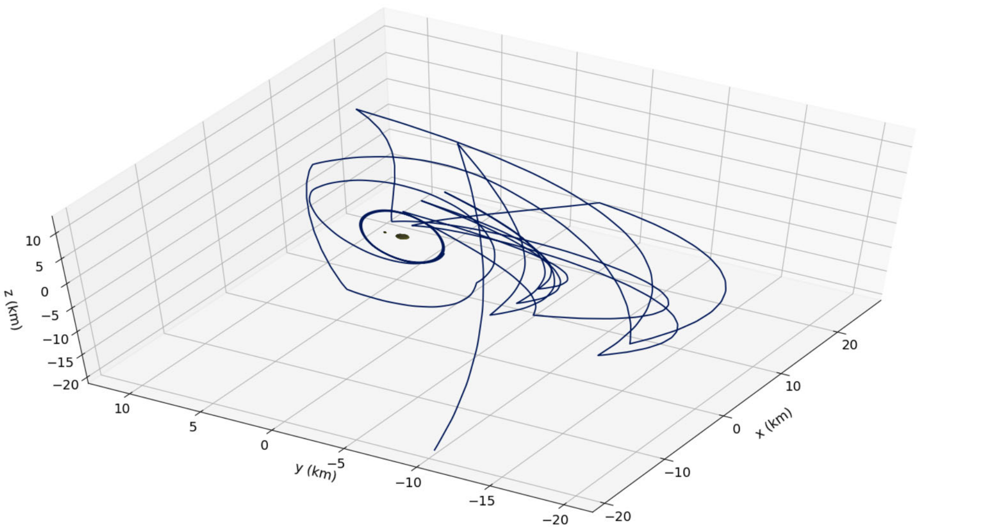

Fig. 17 Milani's trajectory during the nominal and extended asteroid phases. By the end of the mission, Milani is also expected to land on one of the two asteroids

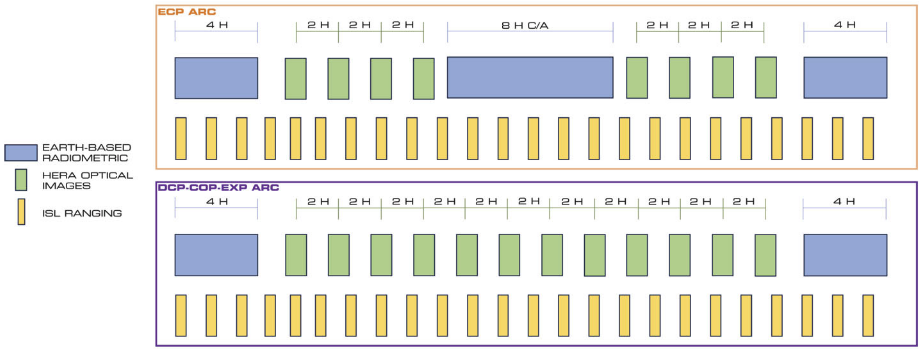

Fig. 18 Hera data acquisition for the asteroid phase. The top panel shows the data collected during the ECP arcs, while the bottom panel covers the DCP-COP-EXP arcs. The main distinction lies in the closest approach: Earth-based Doppler tracking is used during the ECP arcs, while optical images are utilized in the other phases due to the Hera AFC camera's constraint to point towards the asteroids for autonomous navigation. Hera AFC images are conservatively planned to be taken every two hours, though more frequent imaging is expected. ISL ranging data will be collected during specific RSE slots, each lasting a minimum of five minutes (the exact planning is still to be finalized). LIDAR observations, while not included in this particular scheme, will be carried out throughout each arc whenever feasible

of Hera shall point at the target to allow for autonomous navigation, creating a conflict with the pointing requirements of the high-gain antenna.

Optical images from the Hera AFC camera are assumed every 2 hours when the radiometric tracking is inactive (due to pointing constraints), which represents a conservative assumption with respect to the likely mission operations. Regarding the range, the measurements are collected every 300 s.

ISL ranging data will be collected starting from the CubeSats' deployment phase and during specific RSE slots, each lasting a minimum of five minutes. The cumulative duty cycle of ISL data is expected to be 40% within each RSE arc, defined as an uninterrupted interval in which Hera and the CubeSat are at rest (no orbital or reaction wheel desaturation maneuvers). The ISL measurements should be evenly distributed across closed orbits (e.g., SSTO) or in various relative geometric configurations with respect to both asteroids, to maximize ground-track coverage and ensure a comprehensive characterization of the global gravity field. The scheduling of the ISL ranging windows will be finalized during the cruise phase, prior to the asteroid encounter.

7 Methods

7.1 Gravity Science and Orbit Determination

Deep space orbit determination aims to obtain the position and velocity (state) of a deep space spacecraft traveling through the solar system, thanks to a variety of radiometric (range, range-rate, Delta-DOR), optical, altimetry, and ISL measurements. In addition, the OD process can be exploited to obtain a deep understanding of the solar system dynamics and scientific information on celestial bodies (gravity science experiments) (Milani and Gronchi 2010). To do so, accurate and complete dynamical and observational mathematical models must be generated, considering the spacecraft, the surrounding bodies and the propagation media. These models are used to propagate the state of the spacecraft (starting from a priori initial conditions) in time and allow to obtain the computed (expected) observables, which are then compared with the real observed measurements, generating the so-called residuals. If the residuals are characterized by a zero mean, Gaussian, white noise, the model and the trajectory of the spacecraft are accurately known. Otherwise, if deterministic signals (signatures) are present in the residuals, the models must be corrected.

OD codes usually compute linear corrections to be applied to the solved-for parameters of the models using a weighted linearized least-squares estimation filter and try to converge to a set of corrected parameters that unequivocally characterize the trajectory of the spacecraft, hence "optimally" fits the observed measurements (Schutz et al. 2004). However, this technique provides a linear solution to a nonlinear problem, hence the steps must be iterated using the latest parameter estimates until the solution converges (Thornton and Border 2003). The differential correction at k-th step is (Milani and Gronchi 2010):

$$\hat{x}_{k+1} = \hat{x}_k + \left(H_k^T W H_k + P_0^{-1}\right)^{-1} \left(H_k^T W(\overline{z} - \hat{z}(\hat{x}_k)) + P_0^{-1}\left(\hat{x}_0 - \hat{x}_k\right)\right), \quad (10)$$

where $\hat{x}_{k+1}$ is the estimated state vector at the end of the k-th iteration, H_k is the partial derivatives matrix of the computed observables with respect to the estimated parameters at the k-th iteration, $\overline{z}$ is the vector of the observed observables, $\hat{z}(\hat{x}_k)$ is the vector of the computed observables at the k-th iteration, W is the measurements weighting matrix, $\hat{x}_0$ is the a priori knowledge of the state vector, and P_0 it the a priori covariance matrix.

Additionally, the solution includes a corresponding covariance matrix, which delineates the formal uncertainty associated with the determined values, defined as $P_{t_0} = \left[H_{t_0}^T W H_{t_0} + P_0^{-1}\right]^{-1}$.

During the orbital phase around Didymos, Hera RSE will use the data outlined in Sect. 3 to (i) determine the motion of Hera, Juventas, and Milani around the Didymos system, enabling the gravity, rotational, and interior structure experiments, and allowing the characterization of this planetary defence test; (ii) determine the Dimorphos' relative orbit and the heliocentric motion of Didymos system. The orbit of the spacecraft and Dimorphos are assessed through the Doppler, optical, LIDAR observables, and ISL. On the contrary, the slower heliocentric motion of Didymos is essentially inferred from Earth-based two-way range and Delta-DOR data.

The radio science data of Hera, Juventas, and Milani will be processed using NASA-JPL's orbit determination program MONTE (Mission Analysis, Operations, and Navigation Toolkit Environment), currently used for the operations of all NASA's space missions managed by JPL (Evans et al. 2018), as well as for radio science data analysis and processing (see e.g. Iess et al. 2014a,b; Zannoni et al. 2020; Casajus et al. 2021, 2022; Zannoni and Tortora 2013; Gramigna et al. 2023; Park et al. 2014, 2016, 2020). MONTE's mathematical formulation and measurement models are detailed in Moyer (1971, 2005).

7.1.1 Dynamical Models

The gravity field outside a planet of mass M and reference radius r_0 can be derived from the spherical harmonic expansion of the gravity potential U in the body fixed-reference frame:

$$U(r,\delta,\lambda) = \frac{\mu}{r}\sum_{l=0}^{\infty}\sum_{m=0}^{l}\left(\frac{r_0}{r}\right)^l P_{lm}(\sin\delta)[C_{lm}\cos(m\lambda) + S_{lm}\sin(m\lambda)], \tag{11}$$

where $\mu = GM$ is the gravitational parameter of the body, (r, δ, λ) a set of spherical coordinates, P_{lm} are the Associated Legendre Functions, while C_{lm} and S_{lm} are the unnormalized gravity field harmonic coefficients, also called Stokes coefficients. Specifying the Stokes coefficients fully defines the external gravitational potential of the body, which in turn provides information on its internal mass distribution, although the mass distribution itself is not uniquely determined by them.

Within the OD process, all the relevant dynamics must be modeled and updated, namely: the heliocentric orbit of the Didymos system, the relative orbits of Didymos and Dimorphos around their common barycenter, and the relative orbits of Hera, Juventas, and Milani with respect to the Didymos system. The primary gravitational forces acting on Didymos barycenter come from the point-mass gravitational perturbations of the Sun, the Moon, the eight planets, and Pluto, whose positions and velocities are taken from DE440 (Park et al. 2021). Furthermore, the force model considers small gravitational perturbations, namely point-mass perturbations from the 16 most massive main-belt asteroids (Farnocchia 2017). In addition, relativistic perturbations are applied for the Sun, the Moon, and the planets based on the Einstein-Infeld-Hoffman formulation (Moyer 2005).

When dealing with low-gravity bodies, the Non-Gravitational Accelerations (NGA) like Solar Radiation Pressure (SRP), Yarkovsky, YORP, and BYORP effects, become dominant. Hence, high-fidelity models are required to properly fit the radio science residuals to ensure that the physical parameters are directly related to physical signals (i.e., avoiding bias in the estimation). More details on our Yarkovsky modelling are provided in Sect. 7.1.3.

7.1.2 The Full Two-Body Problem

The F2BP characterizes the dynamic interplay between two distributions of mass, leading to interconnected translational and rotational movements driven by the gravitational potential shared between irregular mass distributions. The Didymos binary is as an illustration of the F2BP, and the dynamic evolution of the system is particularly influenced by the shapes, initial positions, and orientations of each component, as depicted in Fig. 19.

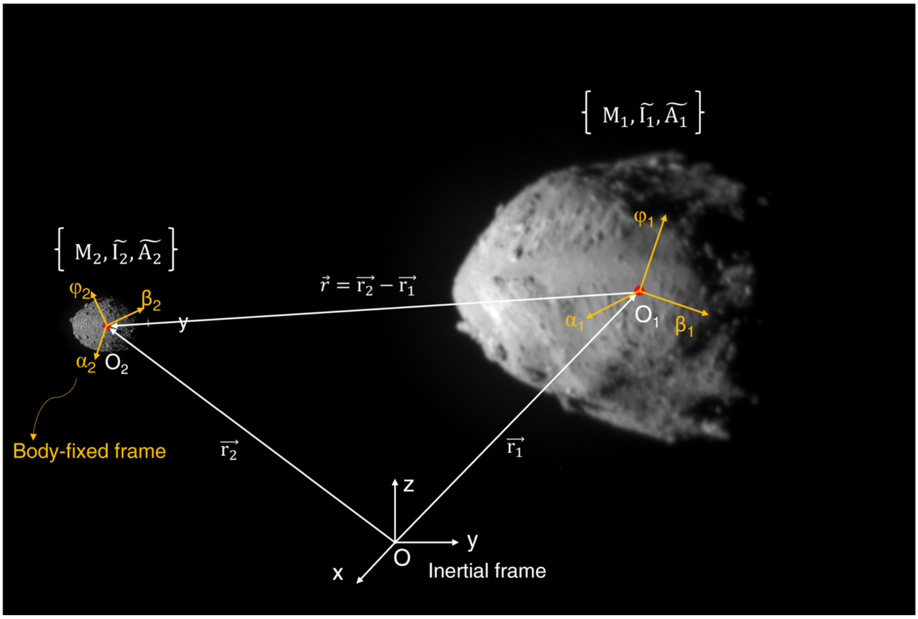

Fig. 19 Full two-body problem model. M_i, I_i, and A_i represent the bodies' masses, inertia moments, and rotation matrices. The image of the Didymos system is from DART DRACO camera mosaics. Image credit: NASA/Johns Hopkins APL, https://dart.jhuapl.edu/Gallery/

The coupling between the translational and rotational motion is usually neglected for most of the planetary science missions targeting larger and more regular bodies since it introduces second-order effects. However, this coupling is expected to be of primary importance for binary asteroid systems, therefore simulation codes specifically designed for the F2BP are required to comprehensively model the intricate dynamics of the system, especially in preparation for the real Hera data analysis.

The F2BP model adopted within the Hera mission is a full 3D model based on Ashenberg (2007), which has been implemented in MONTE. This model relies on Cartesian coordinates, inertia integrals associated with the principal reference frames of each body, and the relative rotation matrix. Within this model, the translational and rotational equations of motion are integrated in a fully coupled manner. In particular, the mutual gravitational potential is described by Equation (12), where subscripts 1 and 2 refer to the primary and secondary body, respectively, while (l, m, n) represent the direction cosines of their relative position vector in the 2 body frames.

$$
\begin{aligned}
U = & \underbrace{-\frac{GM_1M_2}{d}}_{U^{(0)}} - \frac{GM_2}{2d^3}[I_{1xx} + I_{1yy} + I_{1zz} - 3(l_1(I_{1xx}l_1 + I_{1xy}m_1 + I_{1xz}n_1)+ \\
& + m_1(I_{1xy}l_1 + I_{1yy}m_1 + I_{1yz}n_1) + n_1(I_{1xz}l_1 + I_{1yz}m_1 + I_{1zz}n_1))]+ \\
& - \frac{GM_1}{2d^3}[I_{2xx} + I_{2yy} + I_{2zz} - 3(l_2(I_{2xx}l_2 + I_{2xy}m_2 + I_{2xz}n_2)+ \\
& + m_2(I_{2xy}l_2 + I_{2yy}m_2 + I_{2yz}n_2) + n_2(I_{2xz}l_2 + I_{2yz}m_2 + I_{2zz}n_2))].
\end{aligned} \tag{12}
$$

In Equation (12) one can note the zeroth-order potential $U^{(0)}$ term, that is the point mass contribution, while the remaining terms form the second-order potential $U^{(2)}$. Moreover, $U^{(1)}$ captures the influence of a potential discrepancy in the positions of the origins and the centers of mass and presents the first-order effect of this bias. Since we align the origins precisely with the centers of mass in this scenario, $U^{(1)}$ equals zero and it is not reported.

Regarding the rotational integration, the system comprises seven equations: four for the quaternion components and three for the angular velocity components. The external gravity-gradient torques acting on Didymos and Dimorphos are included in the dynamics. The gravity-gradient torque, expressed in the inertial frame, can be written as:

$$\vec{\tau}_i = -\sum_{n=1}^{3} \vec{a}_n \times \frac{\partial U}{\partial \vec{a}_n}, \tag{13}$$

where $\times$ denotes the vector cross product and $\vec{a}_n$ are the column vectors of the rotation matrix from the body-fixed frame to the inertial frame. The time-dependent body-fixed frame estimated parameters include right ascension, declination, prime meridian, and the three angular velocity components, with respect to the inertial frame.

The primary advantages of the F2BP model over the standard radio science approach are twofold. First, it enables the direct estimation of the moments of inertia without requiring constraints on rotational states. Second, from a mathematical perspective, it allows for the direct inclusion of all correlations between the moments of inertia and the estimated parameters. The choice between adopting the F2BP or the standard approach will depend on selecting the model that best fits the data during the operational mission.

7.1.3 Non-gravitational Accelerations and Ephemerides

Estimating the heliocentric trajectory of Didymos and characterizing the momentum enhancement factor from DART's impact $\beta_\odot$ requires including in the OD setup all relevant forces acting on the system. One of the major NGA acting on small bodies is the Yarkovsky effect, which is due to the anisotropic emission of thermal radiation from a rotating body heated by the Sun (Bedini and Tommei 2024). This NGA causes a secular trend in the semi-major axis, which increases for prograde rotators and decreases for retrograde rotators. Previous studies have modeled this effect as a power law of the heliocentric distance according to Equation (14), where A_2 is the acceleration magnitude at a unit distance, r_n is the normalized heliocentric distance, and the exponent d can vary between 0.5 and 3.5 (Farnocchia et al. 2013; Makadia et al. 2022).

$$a_t = A_2 {r_n}^{-d} \tag{14}$$

Equation (14) fully captures the average semi-major axis drift under the assumption that the radial component is symmetric about the perihelion (Chesley et al. 2014). While this simple formulation can fit Earth-based optical astrometry, previous studies have shown that this is not adequate to match the tight constraints of stellar occultations or high-accuracy radiometric data from small-body orbiters (Farnocchia et al. 2021). Higher-fidelity formulations for the Yarkovsky effect approximate the asteroid shape as a sphere and exploit a linearized solution of the heat-transfer equation to model the *Diurnal* and *Seasonal* contributions to the asteroid NGA (Vokrouhlicky 1998; Vokrouhlickỳ and Farinella 1999). These models were tested and compared in a recent study, where we estimated the expected accuracy for the Didymos ephemeris reconstruction using ground-based astrometry, stellar occultations, and Hera radiometric data collected during the asteroid proximity phase. Specifically, range and Delta-DOR data were reduced to *normal points* using as input the Hera relative trajectory around Didymos, which was reconstructed using only Doppler and optical navigation images within the OD process. The approach of decoupling the relative motion of an orbiter around a target and its heliocentric motion is a standard approach used for planetary ephemeris reconstruction (Konopliv et al. 2006, 2014, 2018). However, a more accurate (albeit complex) approach is to estimate the relative and absolute motions within a single OD setup to account for cross-correlation effects. Therefore, future analyses will focus on exploring the discrepancies between the two approaches in preparation for the Hera rendezvous with Didymos.

7.1.4 Data Analysis Setup

The expected accuracies in recovering various geophysical parameters of interest are obtained through gravity science covariance simulations (for more details see Sect. 4 of (Gramigna et al. 2024b)), and are conducted using two different setups, both ready for operational data analysis. The first setup employs standard radio science models, where the asteroids' translational motion is decoupled from their rotational motion. In contrast, the second setup uses the F2BP dynamical model, which accounts for the full coupling and integration of both motions (see Sect. 7.1.2).

The main measurements adopted in the Nominal simulation scenario are the Earth-based two-way range and Doppler, Hera optical measurements of surface landmarks on both Didymos and Dimorphos, as well as Dimorphos centroid during ECP, and ISL ranging data (Gramigna et al. 2024b). In addition, Gramigna et al. (2024b) shows a simulation in which they characterize the addition of Hera LIDAR measurements to Didymos and Dimorphos landmarks and crossovers, which is not reported here for brevity.

The measurement schedule adopted in the simulations follows the expected data acquisition described in Sect. 6 and summarized in Fig. 18. In terms of noises, we conservatively assumed an Earth-based Doppler uncertainty of 0.1 mm/s at 60 s integration time. Regarding the Earth-based range, the assumed uncertainty is 1 m, with an estimated measurement bias of 10 m for every tracking pass. The ISL synthetic range-rate data assumes an uncertainty of 0.05 mm/s at 60 s count time. The optical images noises are considered, conservatively, as 2 pixels for both sample and line, which accounts for error terms such as image processing noises, solar illumination conditions, image geometry, landmarks features.

Furthermore, stochastic accelerations are included for all spacecraft to account primarily for Thermal Recoil Pressure (TRP) and other non-gravitational effects not explicitly modeled in this work (e.g., albedo and thermal emission from the asteroids). These accelerations are estimated with a batch time of 18 hours (corresponding, on average, to one quarter of each arc) and a magnitude of $5 \cdot 10^{-12}$ km/s^2, i.e., approximately 5% of Hera's SRP. For brevity, the complete OD filter configuration is not reported here; the reader is referred to Sect. 7 of Gramigna et al. (2024b) for full details.

Regarding the real radio science data analysis, in order to achieve a precise orbit determination, measurements must be quantitatively calculated before being compared to the observed values. The spacecraft's trajectory is a key factor influencing these computed observations, but additional adjustments are necessary to reach the level of precision required for the scientific goals.

Measurement models are employed to account for these influences. For instance, radiometric measurements are strictly dependent on the inertial positions of the antenna phase centers of the spacecraft and the ground station. The spacecraft's antenna phase center, relative to the spacecraft frame, is determined through pre-launch characterization and surveys.

To find its inertial position, it must first be translated relative to the spacecraft's Center of Mass (CoM). The CoM's position within the spacecraft frame varies after each propulsion maneuver, as the use of propellant changes the overall mass distribution. This position will be recalculated by ESA/ESOC's Flight Dynamics team. Any uncorrected errors in the antenna offset could cause apparent Doppler shifts due to centrifugal motion. Telemetry attitude data provides precise inertial orientation of the satellite. The locations of ground stations and their reference points are precisely determined through surveys, but corrections for temporal variations caused by factors such as tidal deformation, ocean loading on the Earth's crust, and plate tectonics must be applied.

Moreover, optical data is largely influenced by the accuracy of the reconstructed camera pointing. This uncertainty during image capture is accounted for by estimating pointing errors for each image, represented by a set of three parameters. All the aforementioned effects must be precisely taken into account during Hera radio science real data analysis.

Finally, the orbit determination process that combines radiometric and optical data must always be iterative. The reconstructed trajectory of the spacecraft serves as input for the opnav team, which produces updated shape models that then serve as input for the OD team. These iterations aim to refine both the reconstructed trajectory and the updated shape models, maximizing the information extracted from the available data.

8 Expected Accuracies

Simulations were conducted to assess the expected accuracies in the main scientific parameters of interest provided by the Hera RSE, adopting the OD setup and measurement schedule described in Sect. 7.1.4. An extract of the expected results is provided herein, for more details and full simulations see Gramigna et al. (2024b).

8.1 Mass, Gravity Field and Rotational State

In this Section we show the results employing standard radio science models. The main results of these simulations are provided in Fig. 20 and Table 4. Figure 20 shows the scientific information carried by each individual spacecraft within the nominal asteroid phase, which is useful to understand how the different orbits impact the retrieved parameters, an important factor when planning the RSE observations. In particular, the results show that Milani helps in partially improving the knowledge of Didymos degree 2, with respect to the Hera-only case. Milani orbits are mostly characterized by high-altitude flybys (see Fig. 17). Hence, it does not improve the knowledge of the degree 3. On the other hand, most of the information content is driven by the Juventas CubeSat, which by orbiting Didymos at closer distances (SSTO at 3.3 and 2.0 km altitude, see Fig. 16) allows retrieving with very high accuracy both degree 2 and 3, and partially degree 4 depending on the ISL duty cycle and performances.

The complete analysis with all the spacecraft combined, represented by the "Nominal" curve in Fig. 20, shows very similar results to the Hera + Juventas scenario. This allows us to conclude that when investigating small bodies, placing a CubeSat orbiting the body at very short distances is crucial for gravity science purposes.

Furthermore, simulations were conducted to assess the influence of each mission phase on the estimation accuracies as the mission progresses. These results, which are shown in Table 4, are based on the Nominal scenario of Fig. 20 (e.g., Earth-based range and range-rate, ISL ranging with both CubeSats, and Hera AFC optical images).

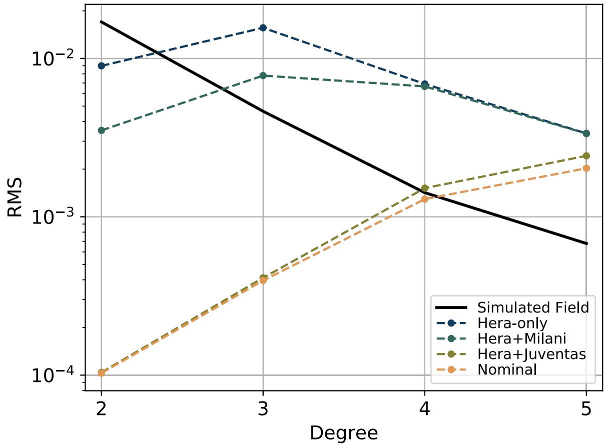

Fig. 20 Power spectra of the simulated Didymos gravity field (black) and of the recovered gravity field uncertainty at the end of the nominal mission showing the contribution of each spacecraft

Table 4 Estimated formal uncertainties (1σ) of Didymos and Dimorphos GM, J_2, relative position, and polynomial pole parameters, at the end of each mission phase. Between squared brackets, the relative uncertainty is displayed

Coefficient	ECP	DCP	COP	EXP
Didymos				
GM (km^3/s^2)	$4.70 \cdot 10^{-11}$	$6.10 \cdot 10^{-12}$	$1.61 \cdot 10^{-12}$	$1.60 \cdot 10^{-12}$
	[0.11%]	[0.015%]	[0.004%]	[0.004%]
J_2	$4.84 \cdot 10^{-2}$	$1.68 \cdot 10^{-4}$	$7.02 \cdot 10^{-5}$	$6.98 \cdot 10^{-5}$
	[57.91%]	[0.20%]	[0.084%]	[0.084%]
α_0 (deg)	3.94	1.90	1.00	0.79
δ_0 (deg)	2.06	1.34	0.82	0.60
Dimorphos				
GM (km^3/s^2)	$7.53 \cdot 10^{-12}$	$8.37 \cdot 10^{-13}$	$2.73 \cdot 10^{-13}$	$2.70 \cdot 10^{-13}$
	[2.18%]	[0.24%]	[0.079%]	[0.078%]
J_2	$8.19 \cdot 10^{-1}$	$5.45 \cdot 10^{-3}$	$5.44 \cdot 10^{-3}$	$5.40 \cdot 10^{-3}$
	[not observable]	[6.61%]	[0.82%]	[0.69%]
α_0 (deg)	3.26	2.90	0.33	0.27
δ_0 (deg)	0.85	0.67	0.15	$7.44 \cdot 10^{-2}$
Position uncertainty (average of R, T, N) (m)	R: 0.69	R: 0.29	R: 0.14	R: 0.12
	T: 1.40	T: 1.17	T: 0.62	T: 0.53
	N: 0.99	N: 0.73	N: 0.22	N: 0.18

During the ECP, Hera's considerable distance from the Didymos system only allows for the estimation of Didymos' GM and J_2 with a formal uncertainty of 0.11% and 57.91%, respectively. For Dimorphos, the corresponding value for the GM is 2.18%, while the J_2 is not observable. Transitioning to the DCP, the deployment of CubeSats and utilization of ISL observables result in a one-two order of magnitude improvement in the gravity reconstruction. Didymos GM and J_2 formal uncertainties at the end of the DCP are 0.015% and 0.20%, respectively. Including also the odd order terms, the recovery of Didymos' degree two harmonics exhibits an overall uncertainty of roughly 1%. Within this phase, the J_2 of

Dimorphos becomes observable with a formal uncertainty of 16.6%. The COP phase, thanks to Juventa's 2 km altitude SSTO orbit, further improves the mass and gravity field recovery.

It should be noted that the experimental phase simulated in this work considers only Hera's expected EXP and does not include the CubeSats' EXP. Hera's EXP does not significantly enhance the accuracy of the gravity field obtained during the nominal mission at the end of the COP. Although a couple of EXP flybys occur at lower altitudes compared to the COP flybys, the distance remains too great to substantially improve the information gathered in the earlier phases. In this context, the ISL data from Juventas are crucial, particularly during its orbit at an altitude of 2 km around Didymos.

Nevertheless, the additional Hera low-altitude flybys enable higher resolution optical measurements of the asteroids and their landmarks, resulting in an improved understanding of their rotational dynamics during the Hera's EXP phase, as shown in Table 4. Specifically, most of the pole parameters for Didymos and Dimorphos improve by a factor between 1.2–2.1 compared to the estimations obtained at the end of the COP. The estimation of Dimorphos' libration also improves by a factor between 1.3–1.9 at the end of the EXP (not reported in Table 4 for brevity, see Table 8 of Gramigna et al. (2024b))

Furthermore, Table 4 shows the evolution of the uncertainties in Dimorphos' relative orbit. At the end of the COP, the position uncertainty, provided in Radial Transverse Normal (RTN) components with respect to Didymos, improves by a factor between 2.2 and 4.9 for all the components with respect to the ECP. The final RTN uncertainties at the end of the EXP are in the order of 0.2–0.5 m.

To further enhance the accuracy of the gravity field estimates, Hera flybys or CubeSats orbits at altitudes below 1.5 km would be necessary. Additionally, the CubeSats' experimental phases, such as the planned SSTO for Milani, along with the landing and surface tracking of both CubeSats, will improve the estimates presented in this work. The CubeSats' optical images will provide independent data that, when integrated with other datasets, will further refine parameter estimates. Moreover, tracking ejecta particles, if present (see e.g. Chesley et al. 2020), could improve our understanding of the higher-order gravity fields of Didymos and Dimorphos. Finally, tracking the CubeSats post-landing may be crucial for recovering their rotational state more precisely.

Finally, Gramigna et al. (2024b) demonstrated that the inclusion of LIDAR measurements and crossovers in the nominal solution enables constraining of Hera's orbit during the flybys, resulting in a decreased uncertainty in Hera's position. This improvement in Hera's position uncertainty leads to a higher accuracy in the reconstruction of the relative orbits of the asteroids as well as Didymos' gravity field. The relative improvement provided by the LIDAR and the crossovers estimation in Dimorphos' reconstructed trajectory is approximately 60% for the radial and tangential components and 40% for the normal component. To conclude, the GMs of Didymos and Dimorphos show improvement factors of 1.2 in the LIDAR scenario.

Overall, the retrieved values meet the Hera RSE requirements and objectives outlined in Sect. 2. Consequently, Hera's precise estimations for these parameters will improve our understanding of the kinetic impactor technique for planetary defence and contribute to advancements in binary asteroid science.

8.2 Full Two-Body Results and Moments of Inertia

In this Section, we provide a summary of the results presented in Gramigna et al. (2024b) obtained using the more accurate F2BP dynamical model described in Sect. 7.1.2.

Table 5 Formal uncertainties (1σ) in the main parameters of interest for the Nominal simulation of Sect. 8.1 and the F2BP scenarios

Coefficient	σ_{nominal}	$\sigma_{\text{F2BP pre-impact}}$	$\sigma_{\text{F2BP post-impact}}$
Didymos			
GM (km^3/s^2)	$1.61 \cdot 10^{-12}$	$1.54 \cdot 10^{-12}$	$1.45 \cdot 10^{-12}$
J_2	$7.02 \cdot 10^{-5}$	$2.32 \cdot 10^{-5}$	$2.16 \cdot 10^{-5}$
α_0	1.00	0.37	0.37
δ_0	0.82	0.21	0.21
Dimorphos			
GM (km^3/s^2)	$2.73 \cdot 10^{-13}$	$3.48 \cdot 10^{-13}$	$3.35 \cdot 10^{-13}$
J_2	$5.44 \cdot 10^{-3}$	$5.64 \cdot 10^{-3}$	$4.21 \cdot 10^{-3}$
α_0 (deg)	0.33	0.76	0.72
δ_0 (deg)	0.15	0.31	0.32

The F2BP cases analyzed include the pre- and post-impact scenarios (see Gramigna et al. 2024b), both of which are non-chaotic and similar to the standard radio science case discussed in Sect. 8.1. We present a comparison of the 1σ uncertainties for key parameters relative to the nominal simulation conducted in Sect. 8.1. To ensure a direct comparison between the dynamical models, the F2BP simulation parameters, instrument performance, ISL duty cycle, measurement noise/models, and spacecraft stochastic accelerations are kept identical to those in the nominal case from Sect. 8.1. In particular, the uncertainties on degree-2 gravity terms are here derived via filter constraints involving the moments of inertia, as per Equation (2).

Table 5 summarizes the uncertainties for GM, J_2 and pole parameters across the different analyzed cases. Overall, the uncertainties for the bodies' GMs in the F2BP simulations are comparable to those in the nominal simulation from Sect. 8.1, which is expected due to the similar orbits. Variations arise from deviations, relative distance oscillations, and librations induced by the F2BP interactions.

Significant improvements are observed in the J_2 and pole uncertainties for Didymos when using the F2BP model, with a reduction by a factor of approximately 3. In contrast, the estimation uncertainties for Dimorphos' parameters remain consistent with previous simulations, though there is a slight degradation, by a factor of about 2, in the pole parameters.

Furthermore, Table 6 presents our preliminary uncertainties in the moments of inertia for Didymos and Dimorphos. As expected, due to the uniform rotation in the pre-impact scenario, the observability of Didymos' principal inertia moments is quite limited. However, the augmented librational state of Dimorphos in the post-impact scenario significantly enhances the observability of the inertia moments for both asteroids, resulting in relative uncertainties of approximately 13–18% for Didymos and 3–5% for Dimorphos.

Further analysis on the observability of the moments of inertia has been conducted recently. In particular, following the findings published by Pravec et al. (2024), their results indicate that Dimorphos exhibits an excited spin state characterized by Non-Principal Axis (NPA) rotation while being, on average, tidally locked-necessary to match the observed lightcurves. Consequently, Gramigna et al. (2024a) performed covariance analyses to explore more chaotic NPA dynamical scenarios. The results demonstrate that the recovery of the body's moments of inertia improved by up to two orders of magnitude compared to the pre- and post-impact F2BP non-chaotic scenario. Additionally, the degree-2 gravity field improved by a factor of 2.5 in the NPA rotation cases. This improvement is attributed to the

Table 6 Formal uncertainties (1σ) in the moments of inertia given by the F2BP scenarios. The values are rounded to 4 decimal places and provided in $kg \cdot km^2$, while the apriori covariances are unconstrained

Coefficient	Value	F2BP pre-impact	F2BP post-impact
Didymos			
I_{XX}	$2.9221 \cdot 10^{10}$	$5.4572 \cdot 10^{10}$	$5.1878 \cdot 10^{9}$
I_{YY}	$3.1394 \cdot 10^{10}$	$5.4572 \cdot 10^{10}$	$5.1878 \cdot 10^{9}$
I_{ZZ}	$3.9236 \cdot 10^{10}$	$5.4572 \cdot 10^{10}$	$5.1878 \cdot 10^{9}$
I_{XY}	0.00	$1.4205 \cdot 10^{7}$	$1.4000 \cdot 10^{7}$
I_{XZ}	0.00	$4.0777 \cdot 10^{7}$	$4.0777 \cdot 10^{7}$
I_{YZ}	0.00	$3.3463 \cdot 10^{6}$	$3.3642 \cdot 10^{6}$
Dimorphos			
I_{XX}	$1.0781 \cdot 10^{7}$	$7.7777 \cdot 10^{5}$	$5.3560 \cdot 10^{5}$
I_{YY}	$1.1215 \cdot 10^{7}$	$8.0784 \cdot 10^{5}$	$5.5731 \cdot 10^{5}$
I_{ZZ}	$1.5383 \cdot 10^{7}$	$1.0647 \cdot 10^{6}$	$7.6387 \cdot 10^{5}$
I_{XY}	0.00	$3.2838 \cdot 10^{3}$	$3.1180 \cdot 10^{3}$
I_{XZ}	0.00	$2.6994 \cdot 10^{4}$	$2.6995 \cdot 10^{4}$
I_{YZ}	0.00	$1.1637 \cdot 10^{4}$	$1.1233 \cdot 10^{4}$

higher observability of the system's dynamic state when in a chaotic and tumbling regime (see Gramigna et al. 2024a for more details).

8.3 Ephemeris and NGA

The expected accuracy of the Didymos ephemeris reconstruction has been assessed in a recent study, which also provides an estimate for the accuracy of the momentum enhancement $\beta_\odot$ and Yarkovsky-related parameters (i.e., A_2 in the power-law model and the Didymos thermal inertia Γ in the Diurnal and Seasonal models). In agreement with previous studies (Makadia et al. 2022), we show that current ground-based data is insufficient to estimate $\beta_\odot$, regardless of the employed NGA model. Adding the Hera radiometric data allows for reducing the asteroid's position uncertainty by roughly two orders of magnitude, reaching m-level accuracy in the orbital radial component and 10 m-level accuracy in the transverse and normal components. The $\beta_\odot$ parameter can now be estimated with a signal-to-noise ratio between 39 for the power-law model and 44 with the analytical model, indicating a minor dependence on the NGA modeling. Additionally, the Hera radiometric data improves the estimation of Yarkovsky-related parameters by a factor of 4 with respect to current data. Therefore, with the data from the Hera mission, we anticipate accurately reconstructing the Didymos heliocentric trajectory and assessing the momentum transferred during a kinetic impact. This will allow us to effectively model and predict the efficacy of future planetary defense missions employing kinetic impactor techniques.

9 Data Archiving and Distribution

Raw data products, including closed-loop and open-loop tracking data in their original form, as provided by ESTRACK and DSN, along with media calibration data, ancillary data, and relevant spacecraft telemetry, will be delivered to the Planetary Science Archive (PSA) for verification and archiving. In particular, ISL ranging data is provided as part of spacecraft telemetry, too. These will be disseminated to the scientific community once verified by PSA reviewers.

Derived data products, such as spherical harmonic coefficients and covariances of the gravitational potential for Didymos and Dimorphos, gravity field maps, spin-pole axes, asteroids' rotational states with covariances, and reconstructed orbits of all spacecraft and asteroids with associated uncertainties, will be archived to the PSA as part of the Hera archival plan. Each data product and bundle will comply with the PDS4 standard and include all necessary documentation.

10 Conclusions

The scope of this paper is to provide a reference for the overall setup of the Hera radio science experiment, providing information on the radio system both for the direct to Earth and ISL, the in-flight operations during cruise and at the Didymos system, and summarize the expected results in geophysics and deep space orbit determination. In combination with several instruments hosted onboard the different Hera mission elements (Hera, Milani, and Juventas), especially the inter-satellite link and optical images, Hera RSE allows improving our knowledge of the mass, gravity field, interior structure, composition, origin, and evolution of Didymos and Dimorphos asteroids, answering many questions left open by the DART impact. This is critical for future planetary defence missions. This work is based on the established hardware configuration, ground test data, and the predictions of the many numerical simulations carried out over the past years.

Acknowledgements PT, EG, RLM, and MZ, wish to acknowledge Caltech and the NASA Jet Propulsion Laboratory for granting the University of Bologna a license to an executable version of MONTE Project Edition S/W. PT, EG, RLM, MZ, GT, GL, RP, and MM are grateful to the Italian Space Agency (ASI) for financial support through Agreement No. 2022-8-HH.0 in the context of ESA's Hera mission.

Funding Information Open access funding provided by Alma Mater Studiorum - Università di Bologna within the CRUI-CARE Agreement.

Declarations

Competing Interests The authors declare that they have no known competing financial interests or personal relationships that could have appeared to influence the work reported in this paper.

References

Agrusa HF, Gkolias I, Tsiganis K, Richardson DC, Meyer AJ, Scheeres DJ, et al (2021) The excited spin state of dimorphos resulting from the dart impact. Icarus 370:114624

Agrusa HF, Zhang Y, Richardson DC, Pravec P, Ćuk M, Michel P, Ballouz R-L, Jacobson SA, Scheeres DJ, Walsh K, Barnouin O, Daly RT, Palmer E, Pajola M, Lucchetti A, Tusberti F, DeMartini JV, Ferrari F, Meyer AJ, Raducan SD, Sánchez P (2024) Direct N-body simulations of satellite formation around small asteroids: insights from DART's encounter with the Didymos system. Planet Sci J 5(2):54. https://doi.org/10.3847/PSJ/ad206b

Ashenberg J (2007) Mutual gravitational potential and torque of solid bodies via inertia integrals. Celest Mech Dyn Astron 99(2):149–159

Asmar SW, Armstrong JW, Iess L, Tortora P (2005) Spacecraft Doppler tracking: noise budget and accuracy achievable in precision radio science observations. Radio Sci 40(2):1–9. https://doi.org/10.1029/2004RS003101

Barbaglio F, Ardito A, Iess L, Madde R, Mercolino M, Lanucara M, Rapino G, et al (2012) Esa δ dor enhancement: agencies interoperability, wideband and low-snr functionality. In: Proceedings of the international astronautical congress, vol 5, pp 3569–3575

Barnouin O, Ballouz R-L, Marchi S, Vincent J-B, Agrusa H, Zhang Y, Ernst CM, Pajola M, Tusberti F, Lucchetti A, Daly RT, Palmer E, Walsh KJ, Michel P, Sunshine JM, Rizos JL, Farnham TL, Richardson DC, Parro LM, Murdoch N, Robin CQ, Hirabayashi M, Kahout T, Asphaug E, Raducan SD, Jutzi M, Ferrari F, Hasselmann PHA, CampoBagatin A, Chabot NL, Li J-Y, Cheng AF, Nolan MC, Stickle AM, Karatekin O, Dotto E, Della Corte V, Mazzotta Epifani E, Rossi A, Gai I, Deshapriya JDP, Bertini I, Zinzi A, Trigo-Rodriguez JM, Beccarelli J, Ivanovski SL, Brucato JR, Poggiali G, Zanotti G, Amoroso M, Capannolo A, Cremonese G, Dall'Ora M, Ieva S, Impresario G, Lavagn M, Modenini D, Palumbo P, Perna D, Pirrotta S, Tortora P, Zannoni M, Rivkin AS (2024) The geology and evolution of the near-Earth binary asteroid system (65803) Didymos. Nat Commun 15(1):6202. https://doi.org/10.1038/s41467-024-50146-x

Bedini L, Tommei G (2024) New Yarkovsky drift detections using astrometric observations of NEAs. Exp Astron 57(1):4. https://doi.org/10.1007/s10686-024-09925-z

Buccino D, Kahan D, Parisi M, Paik M, Barbinis E, Yang O, Park R, Tanner A, Bryant S, Jongeling A (2021) Performance of Earth troposphere calibration measurements with the advanced water vapor radiometer for the Juno gravity science investigation. Radio Sci 56(12):1–9. https://doi.org/10.1029/2021RS007387

Buccino D, Border JS, Folkner WM, Kahan D, Le Maistre S (2022) Low-SNR Doppler data processing for the insight radio science experiment. Remote Sens 14(8):1924. https://doi.org/10.3390/rs14081924

Caldiero A, Le Maistre S (2024) Small bodies global gravity inversion via the level-set method. Icarus 411:115940. https://doi.org/10.1016/j.icarus.2023.115940

Cardarilli GC, Di Nunzio L, Fazzolari R, Giardino D, Matta M, Re M, Iess L, Cialfi F, De Angelis G, Gelfusa D, et al (2019) Hardware prototyping and validation of a w-δdor digital signal processor. Appl Sci 9(14):2909

Casajus LG, Zannoni M, Modenini D, Tortora P, Nimmo F, Van Hoolst T, Buccino D, Oudrhiri K (2021) Updated Europa gravity field and interior structure from a reanalysis of Galileo tracking data. Icarus 358:114187

Casajus LG, Ermakov A, Zannoni M, Keane J, Stevenson D, Buccino D, Durante D, Parisi M, Park R, Tortora P, et al (2022) Gravity field of Ganymede after the Juno extended mission. Geophys Res Lett 49:e2022GL099475

CCSDS (2013) Delta-DOR—Technical Characteristics and Performance. Informational Report, Issue 1, CCSDS 500.1-G-1. https://ccsds.org/Pubs/500x1g1s.pdf

CCSDS (2014) Pseudo-Noise (PN) Ranging Systems. Recommended Standard, Issue 2, CCSDS 414.1-B-2. https://ccsds.org/Pubs/414x1b2s.pdf

Cheng AF, Atchison J, Kantsiper B, Rivkin AS, Stickle A, Reed C, et al (2015) Asteroid impact and deflection assessment mission. Acta Astronaut 115:262–269

Cheng AF, Rivkin AS, Michel P, Atchison J, Barnouin O, Benner L, Chabot NL, Ernst C, Fahnestock EG, Kueppers M, et al (2018) AIDA DART asteroid deflection test: planetary defense and science objectives. Planet Space Sci 157:104–115

Cheng AF, Agrusa HF, Barbee BW, Meyer AJ, Farnham TL, Raducan SD, et al (2023) Momentum transfer from the dart mission kinetic impact on asteroid dimorphos. Nature 616(7957):457–460

Chesley SR, Farnocchia D, Nolan MC, Vokrouhlickỳ D, Chodas PW, Milani A, Spoto F, Rozitis B, Benner LA, Bottke WF, et al (2014) Orbit and bulk density of the OSIRIS-REx target asteroid (101955) Bennu. Icarus 235:5–22

Chesley SR, French AS, Davis AB, Jacobson RA, Brozovic M, Farnocchia D, Lauretta DS (2020) Trajectory estimation for particles observed in the vicinity of (101955) Bennu. J Geophys Res Planets 125(9):2019–006363

Daly M, Barnouin O, Dickinson C, Seabrook J, Johnson C, Cunningham G, Haltigin T, Gaudreau D, Brunet C, Aslam I, et al (2017) The OSIRIS-REx Laser Altimeter (OLA) investigation and instrument. Space Sci Rev 212(1):899–924. https://doi.org/10.1007/s11214-017-0375-3

Dotto E, Zinzi A (2023) Impact observations of asteroid Dimorphos via light Italian CubeSat for imaging of asteroids (LICIACube). Nat Commun 14(1):3055

Dotto E, Della Corte V, Amoroso M, Bertini I, Brucato JR, Capannolo A, et al (2021) LICIACube-the light Italian CubeSat for imaging of asteroids in support of the NASA DART mission towards asteroid (65803) Didymos. Planet Space Sci 199:105185

ECSS (2008) ECSS-E-ST-50-02C - Ranging and Doppler tracking. ESA Requirements and Standards Division. https://ecss.nl/standard/ecss-e-st-50-02c-ranging-and-doppler-tracking/

Evans S, Taber W, Drain T, Smith J, Wu H-C, Guevara M, Sunseri R, Evans J (2018) MONTE: the next generation of mission design and navigation software. CEAS Space J 10(1):79–86. https://doi.org/10.1007/s12567-017-0171-7

Farnocchia D (2017) Small-body perturber files SB431-N16 and SB431-N343. Technical Report IOM 392R-17-005, Jet Propulsion Laboratory

Farnocchia D, Chesley SR, Vokrouhlický D, Milani A, Spoto F, Bottke WF (2013) Near Earth asteroids with measurable Yarkovsky effect. Icarus 224(1):1–13

Farnocchia D, Chesley SR, Takahashi Y, Rozitis B, Vokrouhlický D, Rush BP, et al (2021) Ephemeris and hazard assessment for near-Earth asteroid (101955) Bennu based on OSIRIS-REx data. Icarus 369:114594

Feldhacker JD, Syal MB, Jones BA, Doostan A, McMahon J, Scheeres DJ (2017) Shape dependence of the kinetic deflection of asteroids. J Guid Control Dyn 40(10):2417–2431

Feltens J, Bellei G, Springer T, Kints MV, Zandbergen R, Budnik F, Schönemann E (2018) Tropospheric and ionospheric media calibrations based on global navigation satellite system observation data. J Space Weather Space Clim 8:30

Ferrari F, et al (2021a) Preliminary mission profile of Hera's Milani CubeSat. Adv Space Res 67(6):2010–2029

Ferrari F, et al (2021b) Trajectory options for Hera's Milani CubeSat around (65803) Didymos. J Astronaut Sci 68(4):973–994

Ferrari F, Fodde I, Piccolo F, et al (2026) The scientific operations of Milani NavCam. Space Sci Rev 222

Fiori F, Tortora P, Zannoni M, Ardito A, Menapace M, Bellei G, Budnik F, Morley T, Mercolino M, Orosei R (2022) Deep space orbit determination via Delta-DOR using VLBI antennas. CEAS Space J 14(2):421–430. https://doi.org/10.1007/s12567-022-00424-5

Godard B, Budnik F, Munoz P, Morley T (2015) Orbit determination of Rosetta around comet 67P/Churyumov-Gerasimenko. In: 25th International Symposium on Space Flight Dynamics, Munich, Germany. https://issfd.org/2015/files/downloads/abstracts/124_Godard.pdf

Goldberg HR, Karatekin Ö, Ritter B, Herique A, Tortora P, Prioroc C, et al (2019) The Juventas CubeSat in support of ESA's Hera Mission to the asteroid Didymos

Goldreich P (2009) Tidal evolution of rubble piles. Astrophys J 691(1):54

Gramigna E, Johansen JG, Manghi RL, Magalhães J, Zannoni M, Tortora P, et al (2022) Hera inter-satellite link Doppler characterization for Didymos gravity science experiments. In: 2022 IEEE 9th international workshop on metrology for AeroSpace (MetroAeroSpace). IEEE, pp 430–435

Gramigna E, Parisi M, Buccino D, Casajus LG, Zannoni M, Bourgoin A, Tortora P, Oudrhiri K (2023) Analysis of NASA's DSN Venus Express radio occultation data for year 2014. Adv Space Res 71(1):1198–1215

Gramigna E, Manghi RL, Zannoni M, et al (2024a) Hera orbit determination covariance analysis of Didymos binary asteroid with the full two-body problem. In: 2024 AAS/AIAA astrodynamics specialist conference, p AAS 2024-406

Gramigna E, Manghi RL, Zannoni M, Tortora P, Park RS, Tommei G, et al (2024b) The Hera radio science experiment at Didymos. Planet Space Sci 246:105906

Iess L, Puyuelo RA, Ardito A, Comoretto G, Lanucara M, Maddè R, Mercolino M, Rapino G, Sensi M, Tortora P (2006) The European delta-DOR correlator. In: 57th international astronautical congress, pp 3–1

Iess L, Di Benedetto M, James N, Mercolino M, Simone L, Tortora P (2014a) Astra: interdisciplinary study on enhancement of the end-to-end accuracy for spacecraft tracking techniques. Acta Astronaut 94(2):699–707

Iess L, Stevenson D, Parisi M, Hemingway D, Jacobson R, Lunine J, Nimmo F, Armstrong J, Asmar S, Ducci M, et al (2014b) The gravity field and interior structure of Enceladus. Science 344(6179):78–80

Ivanov BA, Hartmann WK (2007) Exogenic dynamics, cratering and surface ages. Planets Moons 10:207–242

Jacobson SA, Scheeres DJ (2011) Dynamics of rotationally fissioned asteroids: source of observed small asteroid systems. Icarus 214(1):161–178

James N, Abello R, Lanucara M, Mercolino M, Maddè R (2009) Implementation of an ESA delta-DOR capability. Acta Astronaut 64(11–12):1041–1049

Karatekin Ö, Le Bras E, Herique A, Tortora P, Ritter B, Scoubeau M, Moreno VM (2021) Juventas CubeSat for the Hera mission. In: European Planetary Science Congress, pp 2021–750

Konopliv AS, et al (2006) A global solution for the Mars static and seasonal gravity, Mars orientation, Phobos and Deimos masses, and Mars ephemeris. Icarus 182:23–50

Konopliv A, Asmar S, Park R, Bills B, Centinello F, Chamberlin A, Ermakov A, Gaskell R, Rambaux N, Raymond C, et al (2014) The Vesta gravity field, spin pole and rotation period, landmark positions, and ephemeris from the dawn tracking and optical data. Icarus 240:103–117

Konopliv AS, et al (2018) The Ceres gravity field, spin pole, rotation period and orbit from the Dawn radiometric tracking and optical data. Icarus 299(1):411–429

Lasagni Manghi R, Zannoni M, Tortora P, Martellucci A, De Vicente J, Villalvilla J, et al (2021) Performance characterization of esa's tropospheric delay calibration system for advanced radio science experiments. Radio Sci 56(10):1–14. https://doi.org/10.1029/2021RS007330

Lasagni Manghi R, Bernacchia D, Gomez Casajus L, Zannoni M, Tortora P, Martellucci A, et al (2023) Tropospheric delay calibration system performance during the first two BepiColombo solar conjunctions. Radio Sci 58(2):1–15. https://doi.org/10.1029/2022RS007614

Le Maistre S, Rosenblatt P, Rambaux N, Castillo-Rogez JC, Dehant V, Marty JC (2013) Phobos interior from librations determination using Doppler and Star Tracker measurements. Planet Space Sci 85:106–122

Lemoine FG, Smith DE, Rowlands DD, Zuber MT, Neumann GA, Chinn DS, Pavlis EC (2001) An improved solution of the gravity field of Mars (GMM-2B) from Mars Global Surveyor. J Geophys Res Planets 106(E10):23359–23376

Makadia R, Raducan SD, Fahnestock EG, Eggl S (2022) Heliocentric effects of the DART mission on the (65803) Didymos binary asteroid system. Planet Sci J 3(8):184

Mazarico E, Neumann GA, Rowlands DD, Smith DE (2010) Geodetic constraints from multi-beam laser altimeter crossovers. J Geod 84:343–354

Mazarico E, Barker M, Neumann GA, Zuber M, Smith D (2014) Detection of the lunar body tide by the lunar orbiter laser altimeter. Geophys Res Lett 41(7):2282–2288

Mazarico E, Genova A, Neumann GA, Smith DE, Zuber MT (2015) Simulated recovery of Europa's global shape and tidal love numbers from altimetry and radio tracking during a dedicated flyby tour. Geophys Res Lett 42(9):3166–3173

McCarthy LK, Adam CD, Leonard JM, Antresian PG, Nelson D, Sahr E, Pelgrift J, Lessac-Chenen EJ, Geeraert J, Lauretta D (2022) OSIRIS-REx landmark optical navigation performance during orbital and close proximity operations at asteroid Bennu. In: AIAA SciTech 2022 forum, p 2520

Meyer AJ, Scheeres DJ, Agrusa HF, Noiset G, McMahon J, Karatekin Ö, Nakano R (2023) Energy dissipation in synchronous binary asteroids. Icarus 391:115323

Michel P, Küppers M, Bagatin AC, Carry B, Charnoz S, De Leon J, Fitzsimmons A, Gordo P, Green SF, Hérique A, et al (2022) The ESA Hera Mission: detailed characterization of the DART impact outcome and of the binary asteroid (65803) Didymos. Planet Sci J 3(7):160

Michel P, Küppers M, Fitzsimmons A, et al (2025) The Hera space mission in the context of small near-Earth asteroid missions in the past, present and future. Space Sci Rev 221:70. https://doi.org/10.1007/s11214-025-01195-1

Milani A, Gronchi G (2010) Theory of orbit determination. Cambridge University Press, Cambridge

Mizuno T, Kase T, Shiina T, Mita M, Namiki N, Senshu H, Yamada R, Noda H, Kunimori H, Hirata N, et al (2017) Development of the Laser Altimeter (LIDAR) for Hayabusa2. Space Sci Rev 208(1):33–47. https://doi.org/10.1007/s11214-015-0231-2

Moyer TD (1971) Mathematical formulation of the double precision orbit determination program/DPODP. Technical Report JPL-TR-32-1527, Jet Propulsion Laboratory

Moyer TD (2005) Formulation for observed and computed values of Deep Space Network data types for navigation. Wiley, New York

Noda H, Senshu H, Matsumoto K, Namiki N, Mizuno T, Sugita S, Abe S, Araki H, Asari K, Cho Y, et al (2021) Alignment determination of the Hayabusa2 Laser Altimeter (LIDAR). Earth Planets Space 73(1):21

Pajola M, Tusberti F, Lucchetti A, Barnouin O, Cambioni S, Ernst CM, Dotto E, Daly RT, Poggiali G, Hirabayashi M, Nakano R, Epifani EM, Chabot NL, Della Corte V, Rivkin A, Agrusa H, Zhang Y, Penasa L, Ballouz R-L, Ivanovski S, Murdoch N, Rossi A, Robin C, Ieva S, Vincent JB, Ferrari F, Raducan SD, Campo-Bagatin A, Parro L, Benavidez P, Tancredi G, Karatekin Ö, Trigo-Rodriguez JM, Sunshine J, Farnham T, Asphaug E, Deshapriya JDP, Hasselmann PHA, Beccarelli J, Schwartz SR, Abell P, Michel P, Cheng A, Brucato JR, Zinzi A, Amoroso M, Pirrotta S, Impresario G, Bertini I, Capannolo A, Caporali S, Ceresoli M, Cremonese G, Dall'Ora M, Gai I, Casajus LG, Gramigna E, Manghi RL, Lavagna M, Lombardo M, Modenini D, Palumbo P, Perna D, Tortora P, Zannoni M, Zanotti G (2024) Evidence for multi-fragmentation and mass shedding of boulders on rubble-pile binary asteroid system (65803) Didymos. Nat Commun 15(1):6205. https://doi.org/10.1038/s41467-024-50148-9

Park RS, Konopliv AS, Asmar SW, Bills B, Gaskell RW, Raymond CA, Smith DE, Zuber MT (2014) Gravity field expansion in ellipsoidal harmonic and polyhedral internal representations applied to Vesta. Icarus 240:118–132. https://doi.org/10.1016/j.icarus.2013.12.005

Park RS, Konopliv AS, Bills BG, Rambaux N, Castillo-Rogez JC, Raymond CA, Vaughan AT, Ermakov AI, Zuber MT, Fu RR, Toplis MJ, Russell CT, Nathues A, Preusker F (2016) A partially differentiated interior for Ceres deduced from its gravity field and shape. Nature 537:515–517. https://doi.org/10.1038/nature18955

Park RS, Konopliv AS, Ermakov AI, Castillo-Rogez JC, Fu RR, Hughson KHG, Prettyman TH, Raymond CA, Scully JEC, Sizemore HG, Sori MM, Vaughan AT, Mitri G, Schmidt BE, Russell CT (2020) Evidence of non-uniform crust of Ceres from Dawn's high-resolution gravity data. Nat Astron 4:748–755. https://doi.org/10.1038/s41550-020-1019-1

Park RS, Folkner WM, Williams JG, Boggs DH (2021) The JPL planetary and lunar ephemerides DE440 and DE441. Astron J 161(3):105. https://doi.org/10.3847/1538-3881/abd414

Perna D, Barucci MA, Fulchignoni M (2013) The near-Earth objects and their potential threat to our planet. Astron Astrophys Rev 21:65. https://doi.org/10.1007/s00159-013-0065-4

Pravec P, et al (2006) Photometric survey of binary near-Earth asteroids. Icarus 181:63–93

Pravec P, Meyer A, Scheirich P, Scheeres D, Benson C, Agrusa H (2024) Rotational lightcurves of dimorphos and constraints on its post-dart impact spin state. Icarus 418:116138

Ramos-Izquierdo L, Scott VS, Schmidt S, Britt J, Mamakos W, Trunzo R, Cavanaugh J, Miller R (2005) Optical system design and integration of the Mercury laser altimeter. Appl Opt 44(9):1748–1760

Ramos-Izquierdo L, Scott VS III, Connelly J, Schmidt S, Mamakos W, Guzek J, Peters C, Liiva P, Rodriguez M, Cavanaugh J, et al (2009) Optical system design and integration of the lunar orbiter laser altimeter. Appl Opt 48(16):3035–3049

Richardson DC, Walsh KJ (2006) Binary minor planets. Annu Rev Earth Planet Sci 34:47–81

Richardson DC, Agrusa HF, Barbee B, Cueva RH, Ferrari F, Jacobson SA, Makadia R, Meyer AJ, Michel P, Nakano R, Zhang Y, Abell P, Merrill CC, Bagatin AC, Barnouin O, Chabot NL, Cheng AF, Chesley SR, Daly RT, Eggl S, Ernst CM, Fahnestock EG, Farnham TL, Fuentes-Muñoz O, Gramigna E, Hamilton DP, Hirabayashi M, Jutzi M, Lyzhoft J, Manghi RL, McMahon J, Moreno F, Murdoch N, Naidu SP, Palmer EE, Panicucci P, Pou L, Pravec P, Raducan SD, Rivkin AS, Rossi A, Sánchez P, Scheeres DJ, Scheirich P, Schwartz SR, Souami D, Tancredi G, Tanga P, Tortora P, Trigo-Rodríguez JM, Tsiganis K, Wimarsson J, Zannoni M (2024) The dynamical state of the Didymos system before and after the DART impact. Planet Sci J 5(8):182. https://doi.org/10.3847/PSJ/ad62f5

Riley WJ (2008) Handbook of frequency stability analysis. US Department of Commerce, National Institute of Standards and Technology, Boulder

Rowlands DD, Pavlis DE, Lemoine FG, Neumann GA, Luthcke SB (1999) The use of laser altimetry in the orbit and attitude determination of Mars Global Surveyor. Geophys Res Lett 26(9):1191–1194

Scheeres DJ, French AS, Tricarico P, Chesley SR, Takahashi Y, Farnocchia D, McMahon JW, Brack DN, Davis AB, Ballouz R-L, Jawin ER, Rozitis B, Emery JP, Ryan AJ, Park RS, Rush BP, Mastrodemos N, Kennedy BM, Bellerose J, Lubey DP, Velez D, Vaughan AT, Leonard JM, Geeraert J, Page B, Antreasian P, Mazarico E, Getzandanner K, Rowlands D, Moreau MC, Small J, Highsmith DE, Goossens S, Palmer EE, Weirich JR, Gaskell RW, Barnouin OS, Daly MG, Seabrook JA, Asad MMA, Philpott LC, Johnson CL, Hartzell CM, Hamilton VE, Michel P, Walsh KJ, Nolan MC, Lauretta DS (2020) Heterogeneous mass distribution of the rubble-pile asteroid (101955) Bennu. Sci Adv 6(41):3350. https://doi.org/10.1126/sciadv.abc3350

Schutz B, Tapley B, Born GH (2004) Statistical orbit determination. Elsevier, Amsterdam

Thomas CA, Naidu SP, Scheirich P, Moskovitz NA, Pravec P, Chesley SR, et al (2023) Orbital period change of dimorphos due to the dart kinetic impact. Nature 616(7957):448–451

Thornton CL, Border JS (2003) Radiometric tracking techniques for deep-space navigation. Wiley, New York

Tricarico P (2013) Global gravity inversion of bodies with arbitrary shape. Geophys J Int 195(1):260–275

Tricarico P, Scheeres DJ, French AS, McMahon JW, Brack DN, Leonard JM, Antreasian P, Chesley SR, Farnocchia D, Takahashi Y, Mazarico EM, Rowlands D, Highsmith D, Getzandanner K, Moreau M, Johnson CL, Philpott L, Bierhaus EB, Walsh KJ, Barnouin OS, Palmer EE, Weirich JR, Gaskell RW, Daly MG, Seabrook JA, Nolan MC, Lauretta DS (2021) Internal rubble properties of asteroid (101955) Bennu. Icarus 370:114665. https://doi.org/10.1016/j.icarus.2021.114665

Tsuno K, Okumura E, Katsuyama Y, Mizuno T, Hashimoto T, Nakayama M, Yuasa H (2017) Lidar on board asteroid explorer Hayabusa. In: International Conference on Space Optics–ICSO 2006, vol 10567. SPIE, Bellingham, pp 217–223

Vokrouhlicky D (1998) Diurnal Yarkovsky effect as a source of mobility of meter-sized asteroidal fragments. I. Linear theory. Astron Astrophys 335:1093–1100

Vokrouhlickỳ D, Farinella P (1999) The Yarkovsky seasonal effect on asteroidal fragments: a nonlinearized theory for spherical bodies. Astron J 118(6):3049

Wimarsson J, Xiang Z, Ferrari F, Jutzi M, Madeira G, Raducan SD, Sánchez P (2024) Rapid formation of binary asteroid systems post rotational failure: a recipe for making atypically shaped satellites. Icarus 421:116223. https://doi.org/10.1016/j.icarus.2024.116223

Zannoni M, Tortora P (2013) Numerical error in interplanetary orbit determination software. J Guid Control Dyn 36(4):1008–1018

Zannoni M, Tommei G, Modenini D, Tortora P, Mackenzie R, Scoubeau M, Herfort U, Carnelli I (2018) Radio science investigations with the asteroid impact mission. Adv Space Res 62(8):2273–2289

Zannoni M, Hemingway D, Casajus LG, Tortora P (2020) The gravity field and interior structure of dione. Icarus 345:113713

Zhang Y, Michel P, Barnouin OS, Roberts JH, Daly MG, Ballouz R-L, Walsh KJ, Richardson DC, Hartzell CM, Lauretta DS (2022) Inferring interiors and structural history of top-shaped asteroids from external properties of asteroid (101955) Bennu. Nat Commun 13(1):4589. https://doi.org/10.1038/s41467-022-32288-y

Authors and Affiliations

Paolo Tortora[1,2] · Edoardo Gramigna[2] · Riccardo Lasagni Manghi[1,2] · Marco Zannoni[1,2] · Ryan S. Park[3] · Giacomo Tommei[4] · Sebastien Le Maistre[5,6] · Ozgur Karatekin[5] · Giacomo Lari[4] · Roberto Paoli[4] · Maddalena Mochi[4] · Alfonso Caldiero[5] · Paolo Concari[7] · Daniel J. Scheeres[8] · Patrick Michel[9] · Michael Kueppers[10]

✉ P. Tortora
paolo.tortora@unibo.it

1 Dipartimento di Ingegneria Industriale, Alma Mater Studiorum, Università di Bologna, Forlì (FC), 47121, Italy

2 Centro Interdipartimentale di Ricerca Industriale Aerospaziale, Alma Mater Studiorum, Università di Bologna, Forlì (FC), 47121, Italy

3 Jet Propulsion Laboratory, California Institute of Technology, Pasadena, 91011, CA, USA

4 Department of Mathematics, Università di Pisa, Largo Bruno Pontecorvo 5, Pisa, 56127, Italy

5 Royal Observatory of Belgium, Brussels, Belgium

6 Institute for Information and Communication Technologies, Electronics and Applied Mathematics, Université Catholique de Louvain, Av. Georges Lemaitre 4, 1348 Ottignies-Louvain-la-Neuve, Belgium

7 ESA/ESTEC, Noordwijk, The Netherlands

8 University of Colorado Boulder, Boulder, CO, USA

9 Université Côte d'Azur, Observatoire de la Côte d'Azur, CNRS, Laboratoire Lagrange, Nice, France

10 ESA/ESAC, Villanueva de la Cañada, Madrid, Spain